minerals

MDPI

Article

Expanded Insights into Martian Mineralogy: Updated Analysis of Gale Crater's Mineral Composition via CheMin Crystal Chemical Investigations

Shaunna M. Morrison [1,*], David F. Blake [2], Thomas F. Bristow [2], Nicholas Castle [3], Steve J. Chipera [3], Patricia I. Craig [3], Robert T. Downs [4], Ahmed Eleish [1], Robert M. Hazen [1], Johannes M. Meusburger [2], Douglas W. Ming [5], Richard V. Morris [5], Aditi Pandey [5], Anirudh Prabhu [1], Elizabeth B. Rampe [5], Philippe C. Sarrazin [6], Sarah L. Simpson [5], Michael T. Thorpe [7], Allan H. Treiman [8], Valerie Tu [9], Benjamin M. Tutolo [10], David T. Vaniman [3], Ashwin R. Vasavada [11] and Albert S. Yen [11]

1 Earth and Planets Laboratory, Carnegie Institution for Science, Washington, DC 20015, USA; aeleish@ciw.edu (A.E.); rhazen@ciw.edu (R.M.H.); aprabhu@ciw.edu (A.P.)
2 NASA Ames Research Center, Moffett Field, CA 94035, USA; david.blake@nasa.gov (D.F.B.); thomas.f.bristow@nasa.gov (T.F.B.); johannes.m.meusburger@nasa.gov (J.M.M.)
3 Planetary Science Institute, Tucson, AZ 85719, USA; ncastle@psi.edu (N.C.); steve.chipera@gmail.com (S.J.C.); pcraig@psi.edu (P.I.C.); dvaniman@psi.edu (D.T.V.)
4 Department of Geosciences, University of Arizona, Tucson, AZ 85721, USA; rdowns@email.arizona.edu
5 NASA Johnson Space Center, Houston, TX 77058, USA; douglas.w.ming@nasa.gov (D.W.M.); richard.v.morris@nasa.gov (R.V.M.); aditi.pandey@nasa.gov (A.P.); elizabeth.b.rampe@nasa.gov (E.B.R.); sarah.l.simpson@nasa.gov (S.L.S.)
6 eXaminArt, Mountain View, CA 94035, USA; philippe.sarrazin@examinart.com
7 Astronomy Department, Space Flight Center, CRESST II, University of Maryland, Greenbelt, MD 20771, USA; michael.t.thorpe@nasa.gov
8 Lunar and Planetary Institute, Universities Space Research Association, Houston, TX 77058, USA; treiman@lpi.usra.edu
9 Jacobs JETSII at NASA Johnson Space Center, Houston, TX 77058, USA; valerie.m.tu@nasa.gov
10 Department of Earth, Energy, and Environment, University of Calgary, Calgary, AB T2N 1N4, Canada; benjamin.tutolo@ucalgary.ca
11 Jet Propulsion Laboratory, Pasadena, CA 91011, USA; ashwin.r.vasavada@jpl.nasa.gov (A.R.V.); albert.s.yen@jpl.nasa.gov (A.S.Y.)
* Correspondence: smorrison@carnegiescience.edu

Abstract: This study presents mineral composition estimates of rock and sediment samples analyzed with the CheMin X-ray diffraction instrument on board the NASA Mars Science Laboratory rover, *Curiosity*, in Gale crater, Mars. Mineral composition is estimated using crystal-chemically derived algorithms applied to X-ray diffraction data, specifically unit-cell parameters. The mineral groups characterized include those found in major abundance by the CheMin instrument (i.e., feldspar, olivine, pyroxene, and spinel oxide). In addition to estimating the composition of the major mineral phases observed in Gale crater, we place their compositions in a stratigraphic context and provide a comparison to that of martian meteorites. This work provides expanded insights into the mineralogy and chemistry of the martian surface.

Keywords: martian mineralogy; Gale crater; CheMin instrument; Mars Science Laboratory; crystal chemistry; X-ray diffraction; mineral composition

check for updates

Citation: Morrison, S.M.; Blake, D.F.; Bristow, T.F.; Castle, N.; Chipera, S.J.; Craig, P.I.; Downs, R.T.; Eleish, A.; Hazen, R.M.; Meusburger, J.M.; et al. Expanded Insights into Martian Mineralogy: Updated Analysis of Gale Crater's Mineral Composition via CheMin Crystal Chemical Investigations. *Minerals* **2024**, *14*, 773. https://doi.org/10.3390/min14080773

Academic Editors: Dominic Papineau and Roman Skála

Received: 2 May 2024
Revised: 20 July 2024
Accepted: 24 July 2024
Published: 29 July 2024

1. Introduction

Mineralogical exploration of the martian surface has provided invaluable insights into the habitability and geological history of Mars. Gale crater, the landing site of the NASA Mars Science Laboratory (MSL) *Curiosity* rover [1], has been a focal point of investigation due to its unique geologic setting and potential for understanding the past habitability

of Mars. Gale crater is an impact basin formed ~3.8 Ga, and it was subsequently filled with sediment by flowing water over a period of ~200 million years, resulting in layered sedimentary rock representing a large swath of geologic time (~3.8–3.6 Ga for primary emplacement and <3.0 Ga for secondary alteration [2]) during a warmer, wetter period of Mars's history [3,4]. The CheMin (Chemistry and Mineralogy) X-ray diffraction (XRD) instrument on board *Curiosity* plays a crucial role in characterizing the mineralogy of rocks and sediment of Gale crater [5–7]. CheMin has yielded significant scientific findings, including the first definitive detection of water-bearing mineral phases (e.g., clay minerals, gypsum), the prevalence and probable composition of X-ray amorphous materials, and the first and only in situ estimates of martian mineral compositions [3,8–27].

The previous work of Morrison et al. (2018) [8,9] estimated the major element compositions of minerals analyzed by the CheMin instrument in Gale crater, including those of olivine, plagioclase, alkali feldspar, pyroxene, spinel oxide, and alunite–jarosite group minerals. This work developed the method to calibrate the CheMin instrument for these fine-scale measurements and the crystal chemical algorithms with which mineral compositions are estimated [3,7,11,20,21,24,27]. Likewise, these studies provided estimates of the bulk crystalline composition of samples analyzed by CheMin, as well as thresholds on the possible bulk amorphous composition [3,10,11,19,28]. In addition to expanding our understanding of the mineralogy and mineral composition of the martian surface, this prior research provided a foundation on which to explore and better understand the petrological and geologic history of Mars [2,3,10–27,29–63].

In this study, we present an updated analysis of the mineralogy and crystal chemistry of Gale crater based on new samples analyzed by the CheMin instrument. Herein, we provide a comprehensive assessment of the compositions of major crystalline mineral phases (>1–3 wt. % of the total sample; specifically, plagioclase, alkali feldspar, olivine, clinopyroxene, orthopyroxene, and cubic spinel oxides) observed in all the Gale crater samples analyzed by CheMin to date. Through the application of crystal chemical techniques and careful interpretation of the obtained results, this study expands upon our previous research and provides a broader understanding of martian mineralogy and its crucial role in unraveling the geological evolution of Gale crater and Mars at large.

2. Materials and Methods

2.1. CheMin Samples

The CheMin team has analyzed samples from 40 target regions during the traverse through Gale crater and up Aeolis Mons (informally known as Mount Sharp) (Table 1), as of March 2023. The targets are sedimentary in nature, with three being dune fields (i.e., Rocknest, Gobabeb, and Ogunquit Beach) from which the sample sediment was scooped and the other 37 being sedimentary rocks, broadly mudstones, siltstones, and sandstones, which were drilled to produce sample fines <150 μm. Each sample and target region has been characterized according to its membership in the stratigraphic section of Gale crater and Aeolis Mons, lithology, and elevation (Table 1). These samples and their targets represent various fluviolacustrine and eolian environments; for more information on the petrology and geology of the samples and target regions, see the references listed in Table 1. Note that we adopt a concise error notation format to express uncertainties throughout. The notation used is of the form $x(\sigma)$, where x represents the central value of the measurement and σ is the uncertainty in the last digit(s) [e.g., a reported value of 1.10(5) signifies a central value of 1.10 with an uncertainty of $+/-$ 0.05].

Table 1. Gale crater samples analyzed by CheMin, as of March 2023, and their sample settings and characteristics.

Sample	Abbr.	Offset (μm)	Clay Abund. (wt. %)	Total X-ray Amorphous Abundance (wt. %)	Sample Cell	Sols Analyzed	Sample Type	Lithology	Elevation	Depositional Environment	Stratigraphic Unit	Ref.
Rocknest	RN	−53	--	27(14)	7a (Mylar)	94–119	Scoop	Eolian sand	−4516	Modern eolian (inactive)	Bradbury Landing Dune Field	[6,9]
John Klein	JK	−68	22(11)	28(15)	13b (Mylar)	196–273	Drill	Mudstone	−4519	Fluviolacustrine	Yellowknife Bay Formation	[9,24]
Cumberland	CB	−70	18(9)	31(18)	12b (Mylar)	282–432	Drill	Mudstone	−4519	Fluviolacustrine	Yellowknife Bay Formation	[9,24]
Windjana	WJ	−74	8.2(4)	20(11)	13a (Mylar)	623–694	Drill	Sandstone	−4481	Reworked eolian and fluvial	Kimberley Formation	[9,21]
Confidence Hills	CH	−74	7.6(4)	39(15)	12a (Mylar)	765–785	Drill	Mudstone	−4460	Fluviolacustrine	Pahrump Hills, Murray Formation	[9,19]
Mojave 2	MJ	−25	4.7(3)	53(15)	6a (Kapton)	884–944	Drill	Mudstone	−4459	Fluviolacustrine	Pahrump Hills, Murray Formation	[9,19]
Telegraph Peak	TP	−45	--	27(15)	5b (Kapton)	922–949	Drill	Mudstone	−4453	Fluviolacustrine	Pahrump Hills, Murray Formation	[9,19]
Buckskin	BK	−76	--	50(15)	14b (Kapton)	1061–1078	Drill	Mudstone	−4446	Fluviolacustrine	Pahrump Hills, Murray Formation	[9,19]
Big Sky	BS	−26	--	20(10)	7b (Mylar)	1121–1131	Drill	Sandstone	−4434	Ancient eolian	Stimson Formation	[9,25]
Greenhorn	GH	−66	--	65(20)	8a (Mylar)	1139–1148	Drill	Mudstone	−4434	Ancient eolian (halo)	Stimson Formation	[9,25]
Gobabeb	GB	−38	--	34(18)	7a (Mylar)	1262–1280	Scoop	Mudstone	−4423	Ancient eolian (active)	Bagnold Dune Field	[9,10]
Lubango	LB	−75	--	75(25)	8a (Mylar)	1323–1350	Drill	Mudstone	−4429	Ancient eolian (halo)	Stimson Formation	[9,10]
Okoruso	OK	−28	--	35(15)	7b (Mylar)	1334–1346	Drill	Sandstone	−4429	Ancient eolian	Stimson Formation	[9,10]
Oudam	OU	−58	3(2)	36(17)	12a (Mylar)	1362–1398	Drill	Siltstone	−4435	Reworked eolian and fluvial	Hartmann's Valley Member, Murray Formation	[3]
Marimba2	MB	−113	23(12)	40(20)	8b (Mylar)	1425–1436	Drill	Mudstone	−4410	Fluviolacustrine	Karasburg Member, Murray Formation	[3]
Quela	QL	−47	16(8)	52(26)	5a (Kapton)	1470–1480	Drill	Mudstone	−4379	Fluviolacustrine	Karasburg Member, Murray Formation	[3]

Table 1. *Cont.*

Sample	Abbr.	Offset (μm)	Clay Abund. (wt. %)	Total X-ray Amorphous Abundance (wt. %)	Sample Cell	Sols Analyzed	Sample Type	Lithology	Elevation	Depositional Environment	Stratigraphic Unit	Ref.
Sebina	SB	−112	19(10)	51(25)	4b (Kapton)	1496–1507	Drill	Mudstone	−4360	Fluviolacustrine	Sutton Island Member, Murray Formation	[3]
Ogunquit Beach	OG	−89	7(3)	40(20)	1a (Kapton)	1832–1931	Scoop	Eolian sand	−4300	Modern eolian (active)	Bagnold Dune Field	[3]
Duluth	DU	−87	15(7)	35(15)	13b (Mylar)	2061–2095	Drill	Mudstone	−4192	Fluviolacustrine	Blunts Point Member, Vera Rubin Ridge, Murray Formation	[3,29]
Stoer	ST	−110	10(5)	35(15)	10A (Mylar)	2141–2151	Drill	Mudstone	−4169	Fluviolacustrine	Pettegrove Point Member, Vera Rubin Ridge, Murray Formation	[3,29]
Highfield	HF	−81	5(2)	49(15)	10A (Mylar)	2226–2242	Drill	Mudstone	−4147	Fluviolacustrine	Jura Member, Vera Rubin Ridge, Murray Formation	[3,29]
Rockhall	RH	−69	13(6)	34(15)	7b (Mylar)	2264–2284	Drill	Mudstone	−4143	Fluviolacustrine	Jura Member, Vera Rubin Ridge, Murray Formation	[3,29]
Aberlady	AL	−97	28(12)	41(20)	8a (Mylar)	2373–2384	Drill	Mudstone	−4157	Fluviolacustrine	Clay-bearing unit, Jura Member, Murray Formation	[23,27]
Kilmarie	KM	−142	28(12)	44(20)	9b (Mylar)	2388–2400	Drill	Mudstone	−4158	Fluviolacustrine	Clay-bearing unit, Jura Member, Murray Formation	[23,27]
Glen Etive	GE	−107	34(17)	38(19)	8b (Mylar)	2492–2503	Drill	Sandstone	−4133	Fluviolacustrine	Knockfarril Hill Member, Carolyn Shoemaker Formation	[23,27]
Glen Etive 2	GE2	−103	26(13)	37(19)	8a (Mylar)	2543–2555	Drill	Sandstone	−4129	Fluviolacustrine	Knockfarril Hill Member, Carolyn Shoemaker Formation	[23,27]
Hutton	HU	−36	6(2)	38(19)	12a (Mylar)	2672–2678	Drill	Mudstone	−4095	Fluviolacustrine	Glasgow Member, Carolyn Shoemaker Formation	[23]
Edinburgh	EB	−160	7(4)	20(10)	7b (Mylar)	2715–2723	Drill	Sandstone	−4088	Ancient aeolian	Stimson Formation	[23]
Glasgow	GG	−127	24(12)	47(23)	7b (Mylar)	2758–2774	Drill	Mudstone	−4107	Fluviolacustrine	Glasgow Member, Carolyn Shoemaker Formation	[23,27]

Table 1. *Cont.*

Sample	Abbr.	Offset (µm)	Clay Abund. (wt. %)	Total X-ray Amorphous Abundance (wt. %)	Sample Cell	Sols Analyzed	Sample Type	Lithology	Elevation	Depositional Environment	Stratigraphic Unit	Ref.
Mary Anning	MA	−86	28(10)	27(20)	7a (Mylar)	2842–2854	Drill	Sandstone	−4128	Fluviolacustrine	Knockfarril Hill Member, Carolyn Shoemaker Formation	[23,27]
Mary Anning 3	MA3	−74	30(11)	25(19)	7a (Mylar)	2888–2894	Drill	Sandstone	−4128	Fluviolacustrine	Knockfarril Hill Member, Carolyn Shoemaker Formation	[23,27]
Groken	GR	−122	30(16)	26(14)	9a (Mylar)	2912–2930	Drill	Sandstone	−4127	Fluviolacustrine	Knockfarril Hill Member, Carolyn Shoemaker Formation	[23,27]
Nontron	NT	−98	18(8)	40(24)	9a (Mylar)	3058–3077	Drill	Sandstone	−4072	Fluviolacustrine	Mercou Member, Carolyn Shoemaker Formation	[35]
Bardou	BD	−106	12(6)	48(25)	4a (Kapton)	3097–3113	Drill	Sandstone	−4066	Fluviolacustrine	Mercou Member, Carolyn Shoemaker Formation	[35]
Pontours	PT	−114	3(2)	49(25)	1a (Kapton)	3172–3172	Drill	Strong diagenetic overprint—grain size indeterminate	−4041	Fluviolacustrine	Pontours Member, Carolyn Shoemaker Formation	[35]
Maria Gordon	MG	−111	--	54(24)	1a (Kapton)	3232–3232	Drill	Sandstone	−4015	Fluviolacustrine	Dunnideer Member, Mirador Formation	[35]
Zechstein	ZE	−102	--	46(25)	1a (Kapton)	3292–3310	Drill	Sandstone	−3991	Fluviolacustrine	Port Logan Member, Mirador Formation	[35]
Avanavero	AV	5.5	--	58(23)	15a (Kapton)	3517–3520	Drill	Sandstone	−3910	Fluviolacustrine	Contigo Member, Mirador Formation	[35]
Canaima	CA	−42	--	62(23)	15a (Kapton)	3615–3627	Drill	Sandstone	−3879	Fluviolacustrine/Aeolian	Contigo Member, Mirador Formation	[28,35]
Tapo Caparo	TC	−33	--	60(23)	15a (Kapton)	3755–3777	Drill	Mudstone	−3853	Fluviolacustrine	Amapari Member, Mirador Formation	[64,65]

The Rocknest sample was delivered to CheMin several times—in this study, we are analyzing scoop 5 because it was the most thoroughly characterized and is considered to be the most representative of the Rocknest sample location. The John Klein analysis selected was that performed Sols 196–273, as it is the most complete and thoroughly analyzed analysis. The initial analysis of Cumberland, performed for Sols 283–311, was used in this study; the latter analysis (Sols 418–432) had poor grain motion. The indirect vibe analysis of the Gobabeb sample (Sols 1225–1243) was used in this study; the analysis with direct vibration (Sols 1262–1279) resulted in the loss of material from the sample cell and is therefore not representative of the total sample. The Rock Hall abundances and unit-cell parameters were derived from minor frames 1–4, collected in the first analysis (sol 2264). The Oudam, Marimba2, Quela, Sebina, Duluth, Stoer, Highfield, Bardou, Pontours, Maria Gordon, Zechstein, and Canaima samples results are based on the first 15 minor frames because the temperature inside CheMin caused dehydration of gypsum to bassanite in subsequent analyses. The absence of detectable clay minerals is denoted by "--".

2.2. CheMin X-ray Diffraction Data Collection and Processing

The CheMin instrument utilizes X-ray diffraction to identify minerals and X-ray fluorescence (XRF) to measure the elemental composition of the drilled and scooped samples in Gale crater [5]. CheMin analyzed ~75 mm^3 of the <150 μm size fraction of Gale samples, which were delivered to one of the instrument's 27 reusable sample cells arranged in pairs on the sample wheel (Table 1). Sample cell pairs are positioned at the end of a tuning fork, which utilizes piezoelectric actuation to induce convective flow, reducing preferred orientation effects. The sample material is held between two polymer windows (Kapton or Mylar—see Table 1) and positioned with transmission geometry between the microfocus Co X-ray source and an X-ray energy-sensitive charge-coupled device (CCD) detector, with an angular resolution of ~0.35° 2θ FWHM as determined from crystalline standard materials [66]. Two-dimensional (2D) XRD images are collected over 3 to 38 h of analysis. The 2D XRD images are converted to 1D diffraction patterns for analysis and calibrated with beryl–quartz standards, also located on the CheMin sample wheel. The position of each sample cell, relative to the CCD, is calibrated via an internal standard of plagioclase in the analyzed sample material [9]. Additionally, energy-discriminated CoKα diffraction patterns are obtained, and XRF spectra are derived from detected photons to provide qualitative compositional information about the Gale crater samples.

The CheMin instrument has the ability to detect crystalline phases down to ~1 wt. %, depending on the degree of crystallinity and the amount of peak overlap. Major phase (>~5 wt. %) mineral abundances (Table 2; Table S1 in Supplementary Materials contains a machine-readable version of mineral abundances and uncertainties) and unit-cell parameters are quantified and refined through Rietveld refinement of the 1D XRD patterns (Table 3), fitting peak positions, intensities, and breadths using crystallographic information files (CIFs) [67–70]. Abundances of X-ray amorphous, poorly crystalline materials (Table 1) are estimated using a modified version of the FULLPAT program, optimizing the fit between measured CheMin patterns and patterns of individual minerals and X-ray amorphous phases [71,72]. All data collected by the CheMin instrument are available in the Planetary Data System (PDS) Geoscience Node (https://pds-geosciences.wustl.edu/missions/msl/chemin.htm) and the CheMin Database (https://odr.io/chemin).

Table 2. Abundance of crystalline phases detected in Gale crater samples with CheMin. Abundances determined by Rietveld refinement. Uncertainty reported as 1σ. Machine-readable version of table available in Supplementary Materials (Table S1).

Rocknest		**John Klein**		**Cumberland**		**Windjana**		**Confidence Hills**	
Phase	***wt. %***	***Phase***	***wt. %***	***Phase***	***wt. %***	***Phase***	***wt. %***	***Phase***	***wt. %***
Plagioclase	41(3)	Andesine	44(3)	Plagioclase	44(3)	Augite	29(4)	Plagioclase	38(3)
Forsterite	22.4(19)	Pigeonite	11(3)	Pigeonite	16(4)	K-Feldspar	21(4)	Hematite	13.4(9)
Augite	15(3)	Augite	8(3)	Magnetite	8.7(19)	Pigeonite	17(4)	Augite	11.4(18)
Pigeonite	14(3)	Magnetite	7.6(16)	Augite	8(3)	Magnetite	13.8(13)	Pigeonite	10(3)
Magnetite	2.1(8)	Orthopyroxene	6(2)	Orthopyroxene	8(4)	Plagioclase	5.6(14)	K-Feldspar	8.0(13)
Anhydrite	1.5(7)	Forsterite	5.7(15)	Akaganeite	3.4(13)	Forsterite	5.2(14)	Magnetite	6.9(8)
Quartz	1.4(6)	Anhydrite	5.3(14)	Sanidine	3.1(17)	Akaganeite	2.5(12)	Enstatite	5(3)
Sanidine	1.3(13)	Sanidine	2.4(15)	Pyrrhotite	1.9(11)	Anhydrite	1.49(11)	Forsterite	3.3(12)
Hematite	1.1(9)	Akaganeite	2.3(12)	Forsterite	1.8(16)	Pyrrhotite	1.3(8)	Jarosite	1.5(5)
Ilmenite	0.9(9)	Bassanite	2.1(7)	Anhydrite	1.6(12)	Ilmenite	1.1(7)	Ilmenite	1.4(6)
		Pyrrhotite	2.0(9)	Bassanite	1.4(7)	Enstatite	1.0(9)	Quartz	0.8(3)

Table 2. *Cont.*

Rocknest		**John Klein**		**Cumberland**		**Windjana**		**Confidence Hills**	
Phase	***wt. %***	***Phase***	***wt. %***	***Phase***	***wt. %***	***Phase***	***wt. %***	***Phase***	***wt. %***
		Albite	1.3(8)	Hematite	1.3(10)	Hematite	0.9(8)		
		Hematite	1.2(11)	Ilmenite	1.0(9)	Bassanite	0.2(2)		
		Quartz	0.9(9)	Halite	0.2(3)	Quartz	0.2(2)		
		Pyrite	0.6(5)	Quartz	0.2(3)				
		Halite	0.3(3)						
Mojave2		**Telegraph Peak**		**Buckskin**		**Big Sky**		**Greenhorn**	
Phase	***wt. %***	***Phase***	***wt. %***	***Phase***	***wt. %***	***Phase***	***wt. %***	***Phase***	***wt. %***
Plagioclase	55(5)	Plagioclase	38(4)	Plagioclase	43(3)	Plagioclase	47(3)	Plagioclase	42(2)
Pigeonite	13(3)	Opal-Ct	15(3)	Tridymite	34(2)	Pigeonite	19(2)	Magnetite	17.3(10)
Magnetite	6.8(10)	Magnetite	10.9(7)	Sanidine	8.4(18)	Orthopyroxene	14(2)	Anhydrite	16.1(10)
Hematite	7.4(11)	Cristobalite	8.7(7)	Magnetite	6.9(8)	Magnetite	13.1(10)	Orthopyroxene	8(2)
Jarosite	6.8(8)	K-Feldspar	5.9(11)	Cristobalite	6.0(8)	Hematite	2.8(10)	Hematite	6.0(10)
Apatite	4.2(12)	Apatite	3.0(5)	Anhydrite	1.8(6)	Tridymite	1.7(10)	Pigeonite	4.7(10)
Augite	2.6(6)	Enstatite	2.8(11)			Quartz	1.5(3)	Bassanite	4.0(10)
Fe-Forsterite	2.0(13)	Jarosite	2.4(5)			Anhydrite	1.1(00)	Quartz	2.2(10)
Quartz	1.5(6)	Augite	2.1(5)						
Ilmenite	0.9(4)	Hematite	1.6(5)						
		Quartz	1.2(3)						
		Ilmenite	0.9(4)						
		Anhydrite	0.5(2)						
		Bassanite	0.5(3)						
		Opal-Ct	15(3)						
Gobabeb		**Lubango**		**Okoruso**		**Oudam**		**Marimba**	
Phase	***wt. %***	***Phase***	***wt. %***	***Phase***	***wt. %***	***Phase***	***wt. %***	***Phase***	***wt. %***
Plagioclase	36(2)	Plagioclase	43(2)	Plagioclase	42(3)	Plagioclase	51(2)	Plagioclase	46(4)
Olivine	28(2)	Anhydrite	12.3(10)	Pigeonite	21(2)	Hematite	26.0(10)	Hematite	16(2)
Augite	20(2)	Magnetite	11.1(10)	Magnetite	17.3(10)	Pyroxene	10(2)	Anhydrite	10.2(10)
Pigeonite	11(2)	Orthopyroxene	10(2)	Orthopyroxene	11(2)	Anhydrite	5.8(2)	Sanidine	8(3)
Magnetite	2.8(10)	Bassanite	9.0(10)	K-Feldspar	2.9(10)	Gypsum	5.5(10)	Gypsum	6.4(10)
Anhydrite	1.0(2)	Pigeonite	5.9(10)	Apatite	1.6(10)	Quartz	1.9(10)	Forsterite	5(2)
Quartz	0.7(3)	Quartz	3.5(10)	Quartz	1.4(3)			Pyroxene	4(4)
Hematite	0.5(5)	Hematite	2.3(10)	Bassanite	1.2(10)			Bassanite	1.9(10)
		Gypsum	2.3(10)	Hematite	1.1(10)			Jarosite	1.5(10)
				Anhydrite	0.8(10)			Quartz	1.2(10)
Quela		**Sebina**		**Ogunquit Beach**		**Duluth**		**Stoer**	
Phase	***wt. %***	***Phase***	***wt. %***	***Phase***	***wt. %***	***Phase***	***wt. %***	***Phase***	***wt. %***
Plagioclase	44(2)	Plagioclase	38(3)	Plagioclase	47(3)	Plagioclase	55.8(18)	Plagioclase	44.1(17)
Hematite	20(2)	Hematite	20.4(17)	Forsterite	18.2(12)	Hematite	13.0(8)	Hematite	28.3(10)

Table 2. *Cont.*

Quela		**Sebina**		**Ogunquit Beach**		**Duluth**		**Stoer**	
Phase	***wt. %***	***Phase***	***wt. %***	***Phase***	***wt. %***	***Phase***	***wt. %***	***Phase***	***wt. %***
Anhydrite	10.7(10)	Anhydrite	16.9(11)	Augite	15.7(18)	Sanidine	9.0(9)	Pyroxene	7.3(13)
Sanidine	6(2)	Pyroxene	7(4)	Pigeonite	10.2(18)	Pyroxene	9.0(14)	Anhydrite	5.3(5)
Pyroxene	5(2)	Sanidine	5(2)	Magnetite	2.5(6)	Bassanite	5.4(4)	Gypsum	4.2(3)
Forsterite	5(2)	Gypsum	3.8(13)	Hematite	2.3(5)	Anhydrite	3.0(5)	Sanidine	4.0(7)
Bassanite	4.5(10)	Forsterite	3.0(10)	Anhydrite	2.3(5)	Gypsum	1.8(1)	Jarosite	2.2(3)
Gypsum	1.8(10)	Jarosite	2.6(6)	Quartz	1.6(4)	Magnetite	1.6(3)	Akaganeite	1.6(1)
Jarosite	1.4(10)	Bassanite	1.8(5)			Quartz	1.3(2)	Quartz	1.5(3)
Quartz	1.1(10)	Quartz	1.2(6)					Bassanite	0.8(3)
								Magnetite	0.7(2)
Highfield		**Rock Hall**		**Aberlady**		**Kilmarie**		**Glen Etive**	
Phase	***wt. %***	***Phase***	***wt. %***	***Phase***	***wt. %***	***Phase***	***wt. %***	***Phase***	***wt. %***
Plagioclase	47(3)	Plagioclase	38(5)	Plagioclase	35(4)	Plagioclase	33(4)	Plagioclase	40(3)
Hematite	20.2(13)	Anhydrite	21(3)	Anhydrite	19(3)	Anhydrite	29.3(13)	Anhydrite	34.0(13)
Pyroxene	10(4)	Pyroxene	17.1(19)	Bassanite	18.4(14)	Pyroxene	13(5)	Hematite	7(3)
Anhydrite	8.2(10)	Akaganeite	11.3(9)	Pyroxene	15(6)	Bassanite	10.0(10)	Pyroxene	6.0(19)
Gypsum	5.2(10)	Hematite	5.4(4)	Hematite	5.5(14)	Siderite	8.0(10)	Sanidine	5(3)
Sanidine	3.7(10)	Jarosite	4.3(9)	Sanidine	3.9(16)	Hematite	3.8(10)	Bassanite	3.0(12)
Bassanite	2.6(6)	Apatite	2.5(8)	Quartz	2.1(10)	Sanidine	2(2)	Siderite	3.0(9)
Magnetite	1.4(13)			Magnetite	1.9(11)	Quartz	0.8(4)	Quartz	2.0(8)
Quartz	1.3(7)								
Glen Etive 2		**Hutton**		**Edinburgh**		**Glasgow**		**Mary Anning**	
Phase	***wt. %***	***Phase***	***wt. %***	***Phase***	***wt. %***	***Phase***	***wt. %***	***Phase***	***wt. %***
Plagioclase	63(4)	Plagioclase	45(7)	Plagioclase	40(3)	Plagioclase	50(4)	Plagioclase	71(5)
Pyroxene	11(3)	Pyroxene	14(2)	Pyroxene	28(3)	Anhydrite	19(3)	Pyroxene	12(4)
Anhydrite	10.0(6)	Magnetite	12(4)	Magnetite	14.0(18)	Hematite	13(4)	Sanidine	6.3(18)
Sanidine	6.0(15)	Cristobalite	9.3(14)	Fe-Forsterite	12(3)	Pyroxene	6(4)	Anhydrite	3.9(13)
Hematite	4.0(13)	Hematite	4.8(12)	Sanidine	5(3)	Sanidine	4(9)	Fe-Carbonate	3.1(9)
Bassanite	3.0(8)	Sanidine	4.7(12)	Apatite	2.0(13)	Bassanite	3.2(19)	Hematite	2.5(16)
Quartz	2.0(2)	Apatite	3.8(18)	Hematite	0.5(8)	Quartz	3(3)	Quartz	2.1(6)
		Anhydrite	1.2(8)	Quartz	0.2(4)	Apatite	1.0(18)		
						Cristobalite	0.7(10)		
Mary Anning 3		**Groken**		**Nontron**		**Bardou**		**Pontours**	
Phase	***wt. %***	***Phase***	***wt. %***	***Phase***	***wt. %***	***Phase***	***wt. %***	***Phase***	***wt. %***
Plagioclase	64(3)	Plagioclase	57(3)	Plagioclase	51.3(15)	Plagioclase	53.0(18)	Plagioclase	58(5)
Pyroxene	14(6)	Anhydrite	11.4(10)	Hematite	17.1(19)	Hematite	21(3)	Pyroxene	16.7(18)
Sanidine	6(4)	Pyroxene	10(4)	Pyroxene	9(4)	Pyroxene	9(4)	Hematite	9(2)
Bassanite	4.8(5)	Bassanite	7.8(6)	Anhydrite	8(2)	Bassanite	5.5(14)	Sanidine	6(3)
Anhydrite	4.6(12)	Fe-Carbonate	7(3)	Bassanite	5.2(14)	Sanidine	4.2(18)	Bassanite	3.1(16)

Table 2. *Cont.*

Mary Anning 3		**Groken**		**Nontron**		**Bardou**		**Pontours**	
Phase	***wt. %***	***Phase***	***wt. %***	***Phase***	***wt. %***	***Phase***	***wt. %***	***Phase***	***wt. %***
Fe-Carbonate	2.5(17)	Sanidine	4.8(16)	Sanidine	3.7(12)	Ankerite	2.6(18)	Gypsum	2.0(8)
Quartz	2.3(10)	Quartz	1.8(12)	Goethite	2.4(15)	Anhydrite	2.0(14)	Quartz	1.8(10)
Hematite	1.9(5)			Ankerite	2.2(7)	Quartz	1.7(12)	Goethite	1.7(12)
				Quartz	1.5(2)	Gypsum	1.2(8)	Halite	1.2
Maria Gordon		**Zechstein**		**Avanavero**		**Canaima**		**Tapo Caparo**	
Phase	***wt. %***	***Phase***	***wt. %***	***Phase***	***wt. %***	***Phase***	***wt. %***	***Phase***	***wt. %***
Plagioclase	52(4)	Plagioclase	38(4)	Plagioclase	42(6)	Plagioclase	45(4)	Plagioclase	38(4)
Hematite	16(2)	Gypsum	33.7(10)	Hematite	17(5)	Hematite	12(3)	Siderite	26(3)
Pyroxene	7.6(18)	Pyroxene	13(3)	Anhydrite	12(4)	Gypsum	10.5(11)	Pyroxene	22(4)
Alkali Feldspar	6.1(16)	Hematite	10(3)	Goethite	10(4)	Sanidine	8(3)	Kieserite	8(3)
Goethite	6(4)	Bassanite	4.4(8)	Pyroxene	8.7(18)	Pyroxene	8(6)	Bassanite	3.8(18)
Anhydrite	4.8(10)	Quartz	1.9(6)	Bassanite	4.6(12)	Starkeyite	6.1(16)	Anhydrite	2.0(12)
Bassanite	4.4(16)			Sanidine	3.5(18)	Goethite	6(4)		
Gypsum	2.1(10)			Quartz	1.0(10)	Anhydrite	1.6(16)		
Quartz	1.6(8)			Ilmenite	1.0(12)	Quartz	1.3(11)		
						Bassanite	1.1(16)		

2.3. Crystal Chemical Estimation of Mineral Compositions

Morrison et al. (2018) [8] developed crystal chemical algorithms to accurately estimate the major element compositions of abundant mineral phases observed on the martian surface by the CheMin instrument. These predictive algorithms were tailored for Na-Ca plagioclase, alkali feldspar, Fe-Mg olivine, Ca-Mg-Fe clino- and orthopyroxene, alunite–jarosite, and spinel oxide mineral systems. By leveraging crystal chemical relationships established for terrestrial minerals, these algorithms enabled precise estimation of the composition of martian minerals, with unit-cell parameters refined using Rietveld analysis. To develop these algorithms, the authors used least-squares regression and minimization routines to establish relationships between the unit-cell parameters and the chemical compositions of various minerals. For plagioclase phases, they correlated Na-Ca composition with the unit-cell parameters (*a*, *b*, *c*, and β) using a quadratic relationship. Alkali feldspar was examined using a model based on Na-K solid solution—the algorithm accounted for fractional order–disorder in addition to Na-K composition. For Fe-Mg olivine, a linear least-squares regression of Mg and Fe content versus the *b* unit-cell parameter was used. For Ca-Mg-Fe pyroxenes, the linear regression models of augite, pigeonite, and orthopyroxene were refined to minimize the weighted sum of squared errors, resulting in low residual errors for Mg, Fe, and Ca content and thereby the estimated values of sample composition. To characterize the crystal chemical relationships in spinel phases, the authors performed linear regressions of Fe content versus the *a* unit-cell parameter for various spinel compositions (e.g., Fe-Ti, Fe-Cr). Due to the crystallographic limitations of the cubic structure, several possible compositions are reported for each spinel sample. The equations derived for each mineral group allow for the estimation of chemical compositions from X-ray diffraction data alone. These methods assume a specified compositional range for each mineral group (e.g., Na-Ca for plagioclase, K-Na for alkali feldspar, Mg-Fe-Ca for pyroxenes) and do not consider or estimate minor element contributions.

Subsequently, Morrison et al. (2018) [9] applied these algorithms to report the mineral compositions from the CheMin sample locations of Bradbury Landing through Nauklift Plateau (CheMin samples Rocknest through Okoruso). The composition of a mineral specimen is the result of the physical (e.g., temperature and pressure) and chemical (e.g., parent material, fluid influx) conditions of crystallization. Therefore, understanding the chemical composition of minerals provides a greater understanding of the geologic and geochemical environments that existed in Mars's past. These crystal chemical algorithms and supporting mineral data can be found at https://github.com/shaunnamm/regression-and-minimization (accessed on 1 June 2023).

In this work, we utilized the crystal chemical algorithms developed by Morrison et al. (2018) [8] to predict the compositions of Na-Ca plagioclase (Table 3; Figures 1, 2 and 5), alkali feldspar (Table 4; Figures 3–5), Fe-Mg olivine (Table 5; Figure 6), Ca-Mg-Fe clino- and orthopyroxene (Tables 6–8; Figure 7), and spinel oxide (Table 9; Figures 8–10) minerals observed in all Gale crater samples analyzed by CheMin as of March 2023. It should be noted that the compositions of the alunite–jarosite phases are omitted from this study due to their absence in significant quantities (<5 wt. % of the sample) in samples analyzed in post-2018 publications, where their compositions were previously reported. This predictive method, based on crystal chemical relationships established on well-studied natural terrestrial and laboratory-synthesized materials, enables the accurate estimation of mineral compositions on Mars. By applying these predictive methods to the extensive CheMin dataset, we aim to gain valuable insights into the mineralogical trends and geological processes within Gale crater.

2.4. Martian Meteorite Data

To provide greater context for the Gale crater samples, we compared the CheMin-analyzed sample compositions to those of martian meteorites. The compilation of martian meteorite compositions was sourced from Hewins et al. (2016), Papike et al. (2009), Lin et al. (2015), Wittmann et al. (2015), and Nyquist et al. (2016). These studies [73–77] used a combination of analytical techniques to identify minerals and determine their compositions, including scanning electron microscopy (SEM), electron probe microanalysis (EPMA), energy-dispersive X-ray spectroscopy (EDS), and backscattered electron (BSE) imaging. In this paper, we specifically focused on comparing the weight percent oxide information for each relevant mineral phase (i.e., feldspar, olivine, pyroxene, and spinel) between the CheMin mineral samples and the martian meteorite studies. The chemical analyses reported for each sample in these papers are designated only as their broad mineral group (i.e., feldspar, pyroxene). The chemical analyses reported in these studies are broadly categorized by their mineral groups (i.e., feldspar, pyroxene). To further differentiate the feldspar samples into plagioclase feldspar and alkali feldspar, we converted the weight percent oxides into An, Or, and Ab ratios. Samples with alkali components (An and Or) comprising more than 50% were classified as alkali feldspar (Figures 4 and 5). If the Or content was 5% or lower, the sample was included in the plagioclase feldspar category (Figures 2 and 5). All feldspar is assumed to be maskelynitized. Pyroxene phases were not distinguished from one another and were grouped together in a single pyroxene quadrilateral (Figure 7), all spinel phases were shown together in a single violin plot (Figure 9), and all olivine phases were depicted in a single bar plot (Figure 6). Note that these papers report analyses from a diverse range of material types, including *anti-perthitic clasts*, *feldspar crystal clasts*, *granular melt*, *intermediate clasts*, *lithic clasts with zoned pyroxenes*, *microbasaltic (melt rock) clasts*, *monzonitic clasts*, *noritic clasts*, *perthitic feldspar clasts*, *plagioclase clasts*, *poikilitic melt*, *shocked norite*, *spherules*, *sub-ophitic melt*, *veins*, *vitrophyre ameboids*, and *vitrophyre spherules*. While these materials exhibit a diverse array of processes, several of which are not relevant to those of Gale crater—specifically those related to impact—comparing their compositions can still provide valuable insights into their relationships and the geological history of Mars.

3. Results

3.1. Feldspar Group Minerals

Feldspar minerals are the most common rock-forming minerals on Earth and other rocky bodies in our solar system. They largely form through igneous processes and are the most abundant constituent of granite, basalt, and gabbro. They make up most of the crust and mantle of terrestrial planets, including Earth and Mars, as well as the Moon. Understanding their compositions and structures provides insight into a planet's magmatic and volcanic processes, including differentiation, cooling and crystallization rate, and parent material.

3.1.1. Plagioclase Group Minerals

The plagioclase group, a member of the broader feldspar mineral group, consists of the triclinic mineral species anorthite ($CaAl_2Si_2O_8$) and albite ($NaAlSi_3O_8$), with a complete solid solution between the two. Plagioclase compositions are typically reported in terms of the two end-member components, albite (Ab) or anorthite (An), which represent the mol percentage of $NaAlSi_3O_8$ or $CaAl_2Si_2O_8$, respectively.

In this work, we calculate the Ca and Na composition of plagioclase in samples analyzed by CheMin in Gale crater (Table 3; Table S2 in Supplementary Materials contains a machine-readable version of unit-cell parameters, compositions, and associated uncertainties). Our focus lies on samples with sufficiently high plagioclase abundance to allow the refinement of unit-cell parameters, including all of the 40 CheMin samples; however, the Windjana sample had a relatively low abundance of plagioclase (Table 2), resulting in larger uncertainty in the unit-cell parameters and therefore in the estimated composition of Windjana. We assume pure, K-free Na-Ca plagioclase in our compositional estimates to limit the complexity of defining these multidimensional crystal chemical systems (see Section 4.6.1 of *Future Work* below) and because 97.6% of plagioclase/maskelynite analyzed in martian meteorites [73–77] contained <2 wt. % other oxides [9]. Note that Ca and Na are calculated independently and are not constrained to sum to one.

Table 3. Unit-cell parameters and estimated Ca and Na compositions of plagioclase observed in Gale crater samples by the CheMin instrument. Uncertainty reported as 1σ. Machine-readable version of table available in Supplementary Materials (Table S2).

Plagioclase Unit-Cell Parameters and Compositions								
Sample	***a* (Å)**	***b* (Å)**	***c* (Å)**	**α (°)**	**β (°)**	**γ (°)**	**Ca (apfu)**	**Na (apfu)**
RK	8.168(6)	12.863(6)	7.108(4)	93.46(5)	116.22(3)	90.12(3)	0.48(4)	0.51(4)
JK	8.162(5)	12.860(8)	7.108(5)	93.47(5)	116.29(3)	90.10(4)	0.40(4)	0.60(4)
CB	8.162(7)	12.860(8)	7.112(7)	93.42(5)	116.34(4)	90.10(4)	0.32(5)	0.67(5)
WJ	8.17(4)	12.91(9)	7.11(5)	94(1)	116.3(5)	89.9(7)	0.1(7)	0.8(7)
CH	8.166(7)	12.859(7)	7.111(4)	93.44(6)	116.31(4)	90.16(4)	0.38(4)	0.61(4)
MJ2	8.164(4)	12.859(3)	7.110(2)	93.50(4)	116.28(1)	90.10(3)	0.41(3)	0.59(3)
TP	8.157(3)	12.858(6)	7.111(2)	93.47(2)	116.28(2)	90.08(2)	0.36(3)	0.64(3)
BK	8.155(3)	12.862(4)	7.106(4)	93.32(2)	116.28(2)	90.10(2)	0.39(3)	0.62(3)
BS	8.159(8)	12.875(8)	7.103(7)	93.47(6)	116.09(4)	89.97(5)	0.52(5)	0.48(5)
GH	8.165(7)	12.891(9)	7.108(7)	93.24(7)	116.10(4)	90.06(4)	0.38(6)	0.60(6)
GB	8.181(7)	12.868(7)	7.107(6)	93.49(5)	116.19(4)	90.06(3)	0.63(6)	0.36(6)
LB	8.166(11)	12.891(11)	7.111(9)	93.26(10)	116.21(5)	90.04(6)	0.27(8)	0.70(8)
OU	8.163(5)	12.852(7)	7.110(4)	93.52(4)	116.31(4)	90.05(5)	0.41(4)	0.59(4)
OK	8.160(8)	12.880(7)	7.108(6)	93.59(7)	116.17(4)	89.91(6)	0.38(5)	0.61(5)
MB	8.161(7)	12.853(10)	7.112(4)	93.38(6)	116.29(4)	90.10(2)	0.38(4)	0.61(4)
SB	8.162(9)	12.875(19)	7.110(7)	93.41(16)	116.22(7)	90.02(9)	0.36(8)	0.63(8)
QL	8.162(9)	12.875(18)	7.110(7)	93.41(15)	116.22(6)	90.02(9)	0.36(8)	0.63(8)
OG	8.169(6)	12.866(12)	7.107(4)	93.42(2)	116.23(4)	90.17(5)	0.48(5)	0.51(5)
DU	8.165(6)	12.864(6)	7.116(2)	93.46(4)	116.27(2)	90.08(2)	0.34(4)	0.64(4)
ST	8.151(3)	12.865(9)	7.104(5)	93.32(4)	116.23(2)	90.11(2)	0.42(4)	0.60(4)
RH	8.155(5)	12.875(1)	7.113(2)	93.43(5)	116.25(2)	90.15(2)	0.27(3)	0.72(3)

Table 3. *Cont.*

Plagioclase Unit-Cell Parameters and Compositions								
Sample	***a* (Å)**	***b* (Å)**	***c* (Å)**	**α (°)**	**β (°)**	**γ (°)**	**Ca (apfu)**	**Na (apfu)**
HF	8.177(8)	12.879(12)	7.106(3)	92.9(3)	116.33(4)	90.27(3)	0.43(7)	0.56(6)
EB	8.149(10)	12.85(3)	7.109(8)	92.9(3)	116.47(9)	90.17(10)	0.24(8)	0.78(8)
AL	8.176(11)	12.850(11)	7.112(7)	93.41(10)	116.17(5)	90.23(6)	0.59(8)	0.38(8)
KM	8.154(6)	12.871(6)	7.108(7)	93.45(4)	116.17(3)	90.10(3)	0.39(5)	0.61(4)
GE	8.157(5)	12.863(10)	7.107(5)	93.41(13)	116.21(2)	90.13(6)	0.43(4)	0.57(4)
GE2	8.164(6)	12.854(8)	7.110(6)	93.41(4)	116.28(5)	90.10(3)	0.43(5)	0.57(5)
HU	8.163(5)	12.888(4)	7.110(4)	93.51(9)	116.26(4)	90.07(5)	0.25(4)	0.74(4)
GG	8.144(8)	12.841(9)	7.105(5)	93.34(5)	116.24(3)	90.16(3)	0.46(4)	0.56(4)
MA	8.160(3)	12.865(3)	7.109(2)	93.44(2)	116.26(2)	90.11(1)	0.38(3)	0.62(3)
MA3	8.158(5)	12.864(6)	7.110(4)	93.46(5)	116.25(2)	90.13(2)	0.37(4)	0.63(4)
GR	8.162(4)	12.862(3)	7.111(2)	93.48(4)	116.24(2)	90.10(2)	0.40(3)	0.59(3)
NT	8.162(4)	12.872(5)	7.110(3)	93.43(4)	116.22(3)	90.13(2)	0.37(3)	0.62(3)
BD	8.160(8)	12.864(4)	7.108(3)	93.49(3)	116.24(3)	90.09(2)	0.41(4)	0.59(4)
PT	8.159(7)	12.862(6)	7.106(3)	93.44(6)	116.26(4)	90.14(5)	0.43(4)	0.57(4)
MG	8.157(6)	12.860(6)	7.104(4)	93.50(5)	116.22(3)	90.07(2)	0.47(4)	0.54(4)
ZE	8.167(6)	12.867(5)	7.111(5)	93.45(4)	116.26(2)	90.11(3)	0.40(4)	0.59(4)
AV	8.163(2)	12.870(5)	7.108(3)	93.28(4)	116.22(2)	90.19(3)	0.40(3)	0.59(3)
CA	8.152(3)	12.841(9)	7.108(4)	93.49(11)	116.26(5)	90.07(4)	0.43(3)	0.55(3)
TC	8.161(10)	12.862(8)	7.105(2)	93.34(5)	116.14(3)	90.11(11)	0.53(5)	0.47(5)

The plagioclase measured with CheMin in the fluviolacustrine and cemented eolian rock samples of Gale crater, Mars, has a mean composition of An40(9) [$Na_{0.60(9)}Ca_{0.40(9)}Al_{1.40(9)}Si_{2.60(9)}O_8$] (Table 3; Figure 1). The range of composition is An14(68) (Windjana sample) to An59(8) (Aberlady). If we exclude the Windjana sample due to its high uncertainty stemming from its low abundance, the mean Gale plagioclase composition is An40(8) with a range of An24(8) (Edinburgh) to An59(8) (Aberlady). The Yellowknife Bay Formation samples have a mean plagioclase composition of An36(5) and a range of An40(4) (John Klein) to An32(5) (Cumberland). The Murray Formation is the most sampled formation in Gale crater and has a significant variability; the mean Murray plagioclase composition is An39(7), with a range from An27(3) (Rockhall) to An59(8) (Aberlady). Within the Murray Formation, Pahrump Hills samples have a mean of An39(3), Hartmann's Valley Member has a mean of An41(4), Karasburg Member is An37(5), Sutton Island Member is An36(8), and the Vera Rubin Ridge samples have a mean of An39(8). The Stimson Formation has a mean of An35(10), with Big Sky having a notably higher An value at 52(5), whereas Greenhorn, Lubango, Okoruso, and Edinburgh are An38(6), An27(8), An38(5), and An24(8), respectively. The Carolyn Shoemaker Formation has less variability, with a low value of An25(4) (Hutton), a high of An46(4) (Glasgow), and a mean of An39(6). The Mirador Formation samples are close in composition, with a mean of An45(5) and a range of An40(3/4) (Zechstein/Avanavero) to An53(5) (Tapo Caparo).

The Gale crater plagioclase samples analyzed with CheMin have a similar compositional range and mean to those of martian meteorites. Figure 2 displays plagioclase frequency of occurrence by composition [i.e., Ca/(Ca+Na)] for martian meteorites [73–77] and the Gale crater samples. There are 980 martian meteorite plagioclase samples represented in the graph and 40 Gale crater plagioclase samples. Martian meteorites have a range of Ca = 0.02 to Ca = 0.66. Excluding Windjana due to its low abundance and resulting high uncertainty, the Gale samples overall have a range of Ca = 0.24(8) (Edinburgh) to Ca = 0.63(6) (Gobabeb), and the fluviolacustrine and cemented eolian drilled rock samples have a low of Ca = 0.24(8) (Edinburgh) and a high of Ca = 0.59(8) (Aberlady). Martian meteorites have a mean composition of Ca = 0.44(11), and the Gale crater mean is Ca = 0.40(8), excluding Windjana [the overall Gale mean including Windjana is Ca = 0.40(9)].

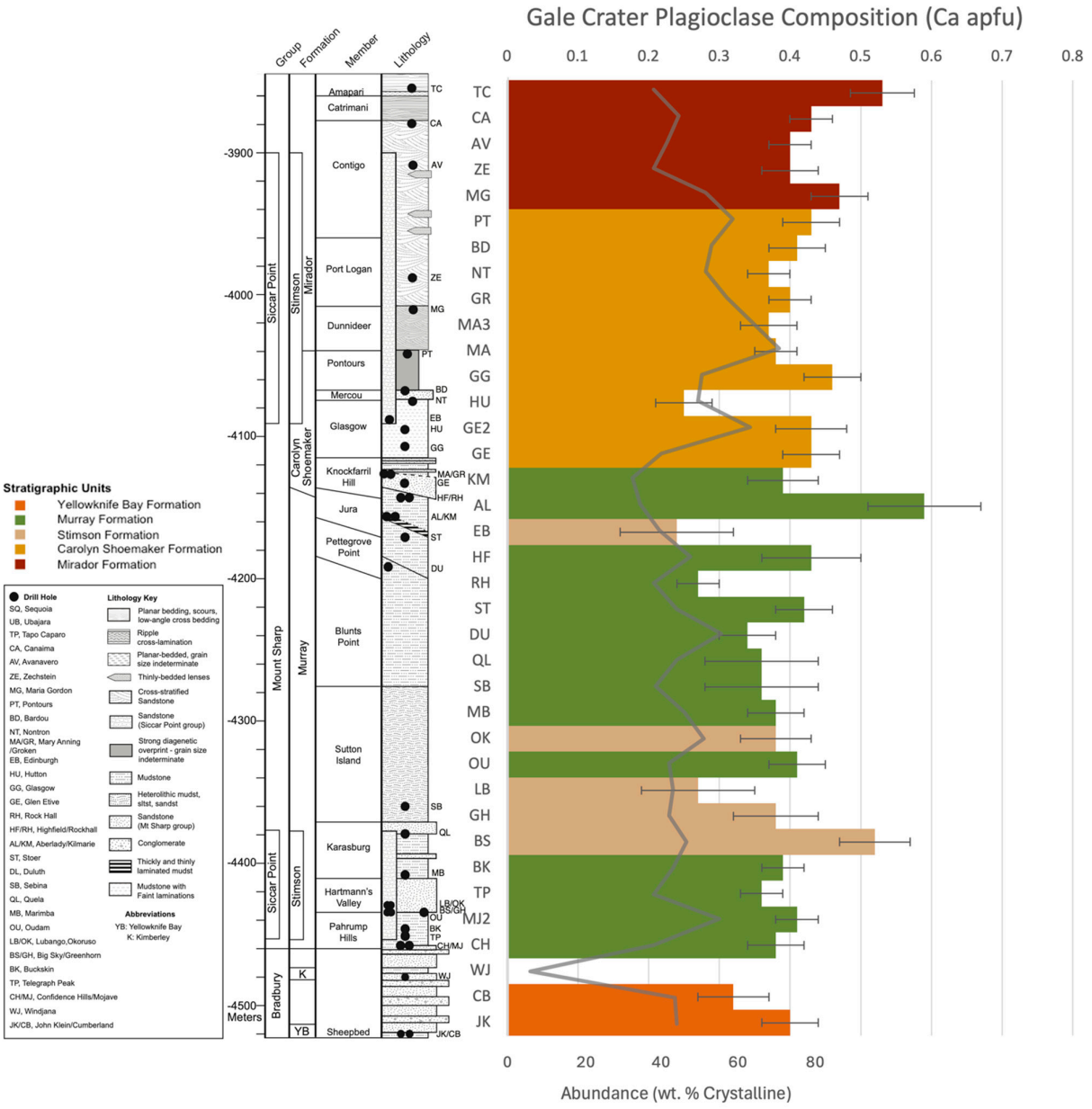

Figure 1. Plagioclase composition (as Ca apfu) of the fluviolacustrine and cemented eolian samples analyzed by the CheMin instrument along the Gale crater stratigraphic section. Error bars represent uncertainty to 1σ. Plagioclase abundance as wt. % of the crystalline sample fraction is displayed as a gray line. The WJ sample was excluded due to its large uncertainty.

3.1.2. Alkali Feldspar Group Minerals

The alkali feldspar group, also a subset of the broader feldspar family, includes four IMA-recognized mineral species: albite ($NaAlSi_3O_8$; triclinic), orthoclase ($KAlSi_3O_8$; monoclinic), microcline ($KAlSi_3O_8$; triclinic), and sanidine ($KAlSi_3O_8$; monoclinic). These end-members display a continuous solid solution series between K and Na, as well as varying degrees of ordering of cations in the structural sites (i.e., the tetrahedral, Al-Si site), resulting in changes to the crystal structure [78]. As with other mineral phases discussed throughout this publication, alkali feldspar composition is the result of the physical and chemical conditions of crystallization. Likewise, the crystallographic site ordering in alkali feldspar is the result of temperature and pressure conditions and cooling rates—higher temperature, lower pressure, and faster cooling result in disordered crystal structures,

whereas lower temperature, higher pressure, and slower cooling rates result in more ordered atomic arrangements. Albite can be ordered (low albite) or disordered (high albite) and is commonly observed in lower-temperature igneous and metamorphic environments. Orthoclase can be fully ordered to partially disordered and is often associated with higher-temperature igneous and metamorphic rocks. Microcline can be fully ordered to partially disordered, most often found in lower-temperature igneous rock such as granite. Sanidine (i.e., high sanidine) is fully disordered and often found in volcanic rock, such as rhyolite.

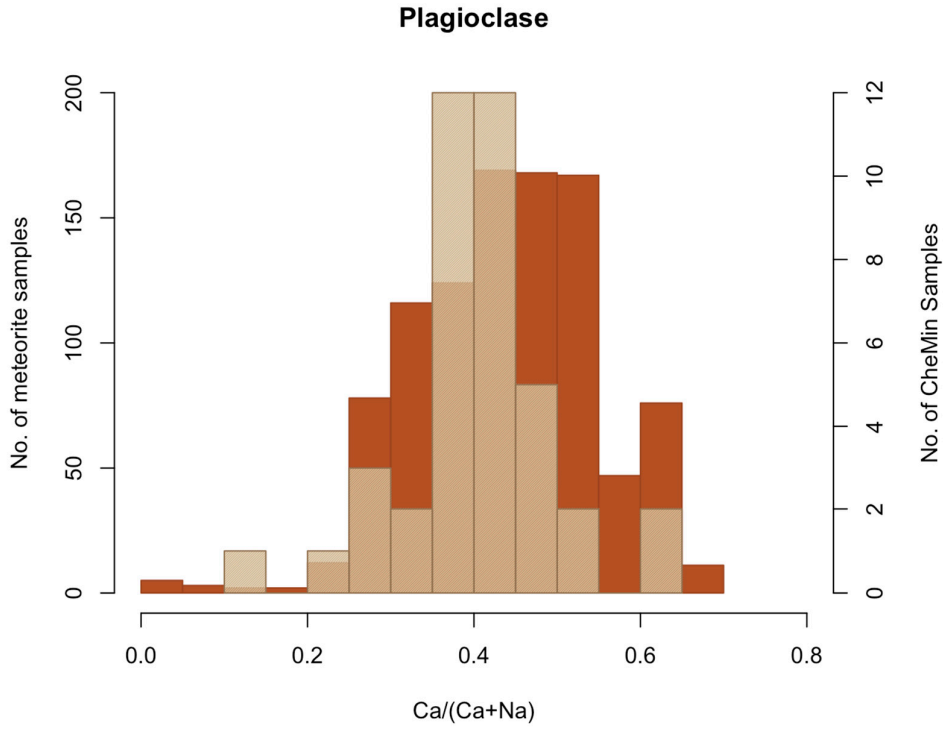

Figure 2. Frequency of occurrence of plagioclase as a function of composition [Ca/(Ca+Na)] in martian meteorites (brown) and Gale crater samples analyzed by CheMin (transparent tan overlay).

For this investigation, we assess the Na composition and ordering state of alkali feldspar in the samples analyzed by CheMin within Gale crater (Figure 3; Table 4; Table S3 of Supplementary Materials contains a machine-readable version of unit-cell parameters, compositions, ordering state, and associated uncertainties). Note that K composition may be calculated by difference from ideal. Our analysis focuses on samples with sufficiently high alkali feldspar abundance to allow for the precise refinement of unit-cell parameters (12 of 40 CheMin samples). Note that this model assumes a composition along the Na-K solid solution and does not account for any potential celsian ($BaAl_2Si_2O_8$) or anorthite ($CaAl_2Si_2O_8$) component—this choice was made in order to limit the complexity of the crystal chemical functions; however, there are likely other chemical components present in minor amounts. In the martian meteorite alkali feldspar analyzed for composition [73–77], CaO was found in abundances up to 10.64 wt. %, BaO up to 2.93 wt. %, and Fe_2O_3 up to 2.67 wt. %, with <1 wt. % other minor oxides including MgO, MnO, TiO_2, and Cr_2O_3 (maximum = 0.70, 0.20, 0.17, 0.02 wt. %, respectively). Only 16% of martian meteorite alkali feldspar contained >1 wt. % of elements other than K, Na, and Ca. While the uncertainty associated with this method can accommodate the incorporation of Ca into the alkali feldspar structure (see Figure 5), the ability of this structure to incorporate several other elements demonstrates the need for a multi-element crystal chemical model for predicting the composition of alkali feldspar (see Section 4.6.1 of *Future Work* below).

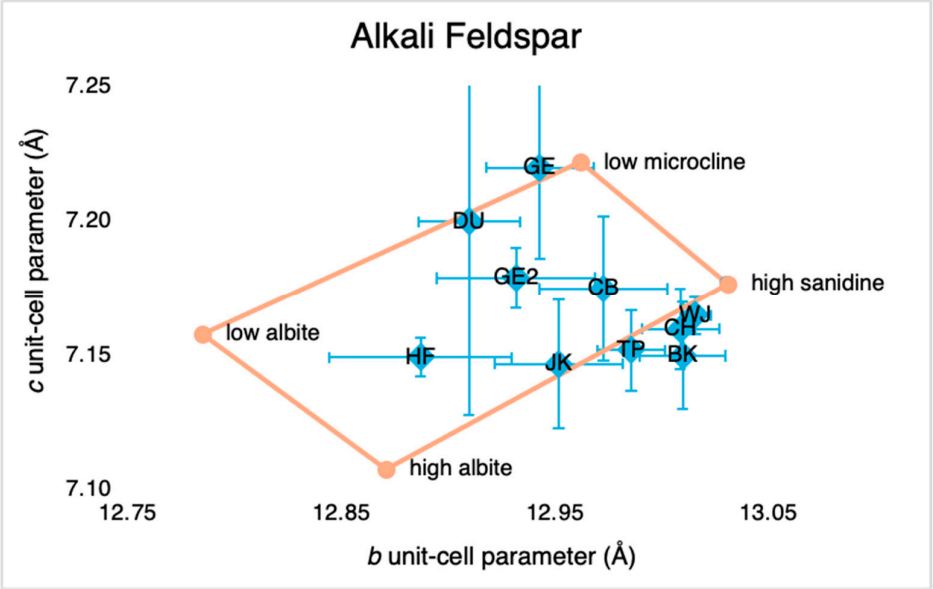

Figure 3. Alkali feldspar unit-cell parameters plotted on the alkali feldspar quadrilateral (*b* unit-cell parameter versus *c* unit-cell parameter, after Morrison et al. (2018) [8,9]. CheMin samples shown in blue, with error bars corresponding to 1σ uncertainty.

Table 4. Unit-cell parameters and estimated Na compositions and ordering state of alkali feldspar observed in Gale crater samples by the CheMin instrument. Uncertainty reported as 1σ. Machine-readable version of table available in Supplementary Materials (Table S3).

Alkali Feldspar Unit-Cell Parameters, Compositions, and Ordering State						
Sample	***a* (Å)**	***b* (Å)**	***c* (Å)**	**β (°)**	**Na (apfu)**	**Ordering**
JK	8.55(3)	12.95(3)	7.15(3)	115.73(14)	0.47(18)	0.1(4)
CB	8.53(3)	12.97(3)	7.18(3)	115.56(18)	0.23(19)	0.3(4)
WJ	8.578(6)	13.016(7)	7.165(7)	116.00(6)	0.13(5)	−0.07(10)
CH	8.584(13)	13.009(18)	7.160(15)	115.96(13)	0.18(11)	−0.1(3)
TP	8.53(2)	12.986(16)	7.152(15)	115.94(17)	0.31(11)	−0.1(3)
BK	8.540(2)	13.01(2)	7.15(2)	115.80(10)	0.23(14)	−0.2(3)
DU	8.62(4)	12.91(3)	7.20(8)	116.2(4)	0.3(5)	1(1)
GE	8.61(8)	12.99(3)	7.24(4)	117(2)	−0.2(3)	1.1(5)
GE2	8.63(5)	12.89(4)	7.149(11)	115.96(8)	0.70(15)	0.5(3)
GG	8.62(3)	12.94(5)	7.22(3)	116.8(6)	0.1(3)	1.1(5)
CA	8.625(5)	12.932(15)	7.179(19)	116.62(14)	0.36(12)	0.6(3)

The abundance of alkali feldspar is relatively low in all samples analyzed by CheMin in Gale crater, with the exception of Windjana [21.1(3.5) wt. % of the crystalline material]. The mean abundance of the CheMin samples, excluding Windjana, is 5.9(26) wt. % of the crystalline material, with a range of 1.7(18) wt. % to 9.0(9) wt. %. The low abundance contributes to higher uncertainty in the refined unit-cell parameters and the derived compositions and ordering states. The alkali feldspar samples measured with CheMin in Gale crater, Mars, have a mean composition of Ab28(18) [$Na_{0.28(18)}K_{0.72(18)}Al_{2)}Si_2O_8$] and an ordering state ranging from fully ordered (1) to fully disordered (0) (Table 4; Figure 3). The range of composition is Ab0(2) (Glen Etive sample) to Ab70(15) (Glen Etive 2). The range of ordering is from −0.24(29) (Buckskin) to 1.08(43) (Glasgow). The Yellowknife Bay Formation samples have a mean alkali feldspar composition of Ab35(18) and a range of Ab23(19) (Cumberland) to Ab47(18) (John Klein); the mean ordering state is 0.18(30), with John Klein being nearly fully disordered at 0.05(36) and Cumberland being partially ordered at 0.31(40). The Kimberley Formation has only one sample, Windjana, but its abundance of alkali feldspar is high [21.1(3.5) wt. % of the crystalline material]; its composition is Ab13(5),

and its ordering state is fully disordered at −0.07(10). The Murray Formation has alkali feldspar reported in 4 of its 14 samples; the mean Murray alkali feldspar composition is Ab26(13), with a range from Ab18(11) (Confidence Hills) to Ab32(43) (Duluth); the mean ordering state is partially ordered at 0.15(57), with a range from fully disordered at −0.24(29) (Buckskin) to fully ordered at 1.01(97) (Duluth). Note that Duluth has higher than mean uncertainty both in composition and ordering state, despite having an abundance, abundance uncertainty, and uncertainty in most unit-cell parameters in line with the mean Gale samples. This could be due to several factors; specifically, (1) its uncertainty in the *c* unit-cell parameter is higher than the mean, or (2) it may contain a chemical element(s) other than K and Na, which this method is not equipped to quantify (see Discussion). Within the Murray Formation, Pahrump Hills samples have a mean composition of Ab26(13) and are fully disordered [mean ordering state = −0.14(16)]. The Carolyn Shoemaker Formation has alkali feldspar reported in 3 of its 10 samples, with a low value of Ab0(2) (Glen Etive sample), a high value of Ab70(15) (Glen Etive 2), and a mean of Ab19(39); the mean ordering state is slightly disordered at 0.87(37), with a range of 0.46(26) (Glen Etive 2) to 1.08(43) (Glasgow). The Mirador Formation has only one reported sample containing alkali feldspar, and that is Canaima with Ab36(12) and partial ordering at 0.27(27).

The Gale crater alkali feldspar samples analyzed with CheMin have a similar compositional range but a distinctly different mean in comparison to martian meteorites (Table 4; Figure 4). The origin of alkali feldspar in martian meteorites is complex and appears to be a combination of primary magmatic processes and subsequent modification by shock and high-temperature impact events [73–77]. Both sodic plagioclase and K-feldspar, along with evidence of perthitic exsolution and reaction rims, have been reported in martian meteorites. The significant amounts of alkali feldspar with subequal amounts of K and Na further indicate compositions quenched well above the solvus, which is rare on Earth but not unprecedented in high-temperature environments [79]. Figure 4 displays alkali feldspar frequency of occurrence by composition [i.e., Na/(K+Na)] for martian meteorites [73–77] and the Gale crater samples. There are 786 martian meteorite alkali feldspar samples represented in the graph and 11 Gale crater alkali feldspar samples. Martian meteorites have a range of Na = 0.06 to Na = 0.98. The Gale samples have a range of Na = 0.00(2) (Glen Etive) to Na = 0.70(15) (Glen Etive 2). Martian meteorites have a mean composition of Na = 0.90(17), and the Gale crater mean is Na = 0.28(18).

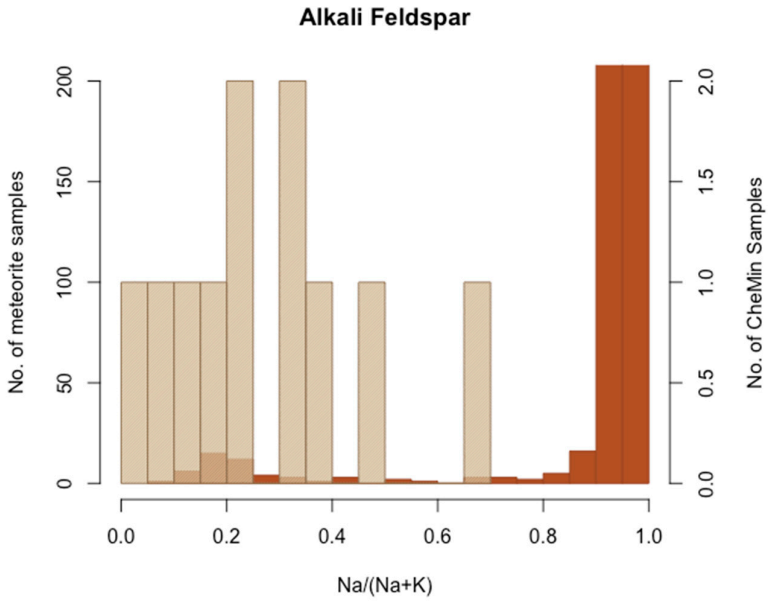

Figure 4. Frequency of occurrence of alkali feldspar as a function of composition [Na/(Na+K)] in martian meteorites (brown) and Gale crater samples analyzed by CheMin (transparent tan overlay).

Figure 5 demonstrates that alkali feldspar has both a wide range of composition and relatively large uncertainties in its compositional values. Even with these large uncertainties, there are no Gale crater alkali feldspar samples with compositions of Ab > 80. Likewise, while plagioclase has significantly lower uncertainty and nearly spans the entire compositional range of martian meteorites, it too does not contain samples with Ab > 80.

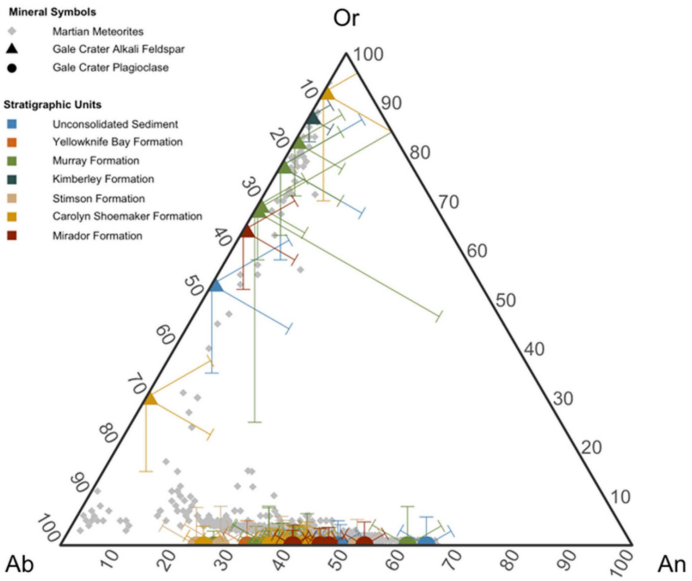

Figure 5. Feldspar composition as a function of Or (% $KAlSi_3O_8$), Ab (% $NaAlSi_3O_8$), and An (% $CaAl_2Si_2O_8$) in martian meteorites and Gale crater samples analyzed by CheMin. Gale crater sample error bars are at 1σ uncertainty.

3.2. Olivine Group Minerals

The olivine group of minerals consists of 22 IMA-approved species, with 8 being silicates. Each of these phases exhibits the characteristic orthorhombic olivine crystal structure, with the most common olivine phases being forsterite (Mg_2SiO_4) and fayalite (Fe_2SiO_4). Mg-Fe olivine is the most abundant constituent of Earth's mantle (i.e., peridotite) and is often found to occur in mafic crustal rocks (i.e., basalt). Similarly, it is a component of many other rocky bodies in our solar system, including Mars, the Moon, and meteorites representing various materials and planets (e.g., chondrites, achondrites, martian meteorites). Forsterite and fayalite exhibit a complete solid solution, wherein Mg can substitute entirely for Fe and vice versa, resulting in a range of intermediate compositions. The compositional variation in this solid solution series is commonly expressed as Fo (forsterite) content, representing the percentage of Mg_2SiO_4 in the mineral. On Earth, olivine typically falls within the range of Fo70 ($Mg_{1.40}Fe_{0.60}SiO_4$) to Fo90 ($Mg_{1.80}Fe_{0.20}SiO_4$).

In this work, we determined the Mg and Fe composition of Mg-Fe olivine group minerals in samples analyzed by CheMin within Gale crater (Table 5; Table S4 in Supplementary Materials contains a machine-readable version of unit-cell parameters, compositions, and associated uncertainties). Note that Mg and Fe are calculated independently and not constrained to sum to 2 apfu. Our analysis is centered on samples with a significant abundance of Mg-Fe olivine, enabling us to accurately refine the unit-cell parameters (7 of 40 CheMin samples). We assume pure, Mn- and Ca-free Mg-Fe olivine in our compositional estimates. We make this assumption in order to limit the computational complexity of the crystal chemical relationships and present an estimation of the abundance of major elements; however, it is likely that minor elements are present in these samples. In martian meteorites [73,77], all samples have a minimum of 0.58 wt. % oxides other than FeO and MgO (i.e., TiO_2, Al_2O_3, Cr_2O_3, MnO, and CaO), a maximum of 2.01 wt. % other oxides, and a mean of 1.03 wt. % other oxides. While it is possible that some of these minor oxides are related to inclusions or beam skirting onto another phase, it is also likely that some minor amount of other elements are present in the Gale olivine samples

(see Section 4.6.1 of *Future Work* below). Understanding the chemical makeup of these olivine phases further enriches our understanding of the igneous processes and geologic conditions that formed martian rocks, shedding light on the planet's past environments and geological evolution.

Table 5. Unit-cell parameters and estimated Mg and Fe compositions of olivine observed in Gale crater samples by the CheMin instrument. Uncertainty reported as 1σ. Machine-readable version of table available in Supplementary Materials (Table S4).

Olivine Unit-Cell Parameters and Compositions					
Sample	***a* (Å)**	***b* (Å)**	***c* (Å)**	**Mg (apfu)**	**Fe (apfu)**
RK	4.785(3)	10.318(4)	6.025(3)	1.14(3)	0.86(3)
JK	4.791(19)	10.289(12)	6.044(16)	1.35(9)	0.65(9)
CB	4.81(4)	10.28(3)	6.03(5)	1.44(15)	0.56(15)
WJ	4.773(7)	10.289(10)	6.006(11)	1.35(7)	0.65(7)
GB	4.785(3)	10.327(3)	6.033(4)	1.08(3)	0.92(3)
OG	4.784(6)	10.311(7)	6.030(6)	1.19(6)	0.81(6)
EB	4.760(4)	10.302(4)	6.017(6)	1.26(3)	0.74(3)

The Gale crater olivine samples analyzed with CheMin have a similar mean but a significantly more limited range of composition relative to martian meteorites (Table 5; Figure 6). Figure 6 displays the olivine frequency of occurrence by composition [i.e., Mg/(Mg+Fe)] for martian meteorites [73,77] and the Gale crater samples. There are 617 martian meteorite olivine samples represented in the graph and 7 Gale crater olivine samples, which include all of the scooped sediment samples analyzed by CheMin. Martian meteorites have a mean composition of Mg = 0.61(16), and the Gale crater overall mean is Mg = 0.63(6). The sediment samples have a lower mean than that of the fluviolacustrine and cemented eolian samples, at Mg = 0.57(3) and Mg = 0.68(5), respectively. Martian meteorites have a range of Mg = 0.17 to Mg = 0.85 and a distinctly bimodal distribution. The cluster of meteorite samples with Mg < 0.45 are all classified as nakhlites (113 samples), whereas the meteorites in the group of samples with Mg < 0.55 are shergottites (459 samples), dunites (36), and clasts from black beauty (NWA 7533; 3 samples). The Gale sample compositions have a range of Mg = 0.54(2) (Gobabeb) to Mg = 0.72(8) (Cumberland) and plot with the high-Mg martian meteorite grouping associated with shergottites, nakhlites, and black beauty.

3.3. Pyroxene Group Minerals

There are 29 IMA-recognized minerals that exhibit the pyroxene structure (RRUFF.info/IMA; data accessed 6 September 2023). Pyroxene minerals are single-chain silicates that form in either the monoclinic (dubbed clinopyroxene) or orthorhombic crystal system (i.e., orthopyroxene). They have the general chemical formula $M2M1Si_2O_6$, where M2 and M1 either are both divalent cations (primarily Ca, Fe^{2+}, Mg) or contain monovalent cations (Na, Li) in the slightly larger *M*2 site and trivalent cations (Al, Fe^{3+}) in the slightly smaller *M*1 site. Pyroxenes are common minerals in mafic igneous rocks (i.e., basalt, gabbro) on Earth, with diopside ($CaMgSi_2O_6$), augite [$(Ca,Mg,Fe)_2Si_2O_6$], and aegirine ($NaFe^{3+}Si_2O_6$) being among the most common, with 4135, 2060, and 1022 localities reported on mindat.org, respectively (https://rruff.info/mineral_list/MED/mineral_locality_count.php; date accessed 6 September 2023). Pyroxene phases are also abundant in meteorites, including martian meteorites, and lunar rocks [80]. Likewise, pyroxenes have also been detected in abundance in Gale crater by the CheMin instrument team [3,9] and via remote sensing [81,82]. These rock-forming minerals are notably sensitive to the temperature and pressure of formation and are therefore used as thermometers and barometers to determine the original conditions of crystallization [9,83,84].

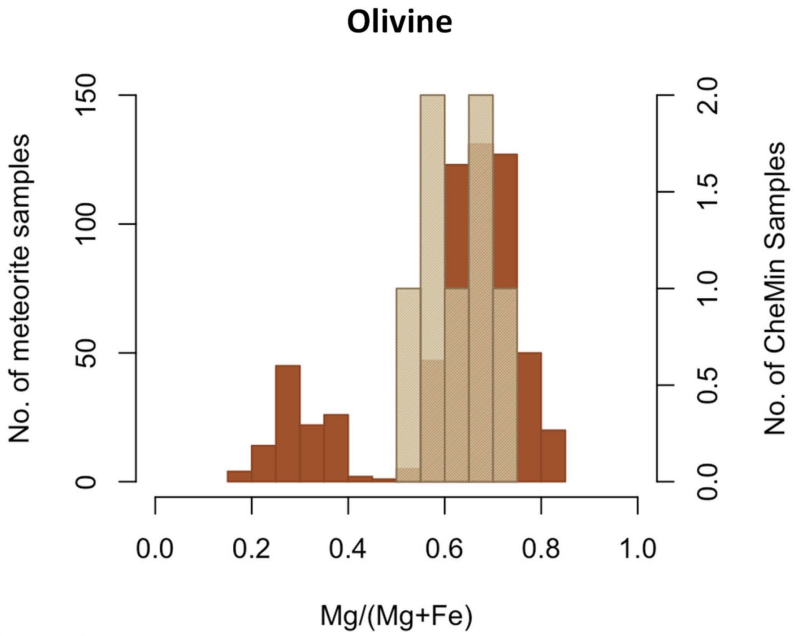

Figure 6. Frequency of occurrence of olivine as a function of composition [Mg/(Mg + Fe)] in martian meteorites (brown) and Gale crater samples analyzed by CheMin (transparent tan overlay).

One or more pyroxene phases were detected in 32 of the 40 Gale crater samples analyzed with the CheMin instrument, specifically augite [$(Ca,Mg,Fe)_2Si_2O_6$], pigeonite [$(Mg,Fe,Ca)_2Si_2O_6$], and an orthopyroxene phase [$(Mg,Fe^{2+}{}_2)Si_2O_6$]. However, due to the overlapping XRD peaks of the various pyroxene phases, it is difficult to accurately refine pyroxene unit-cell parameters of samples when multiple phases are present at the current 2θ resolution of the CheMin instrument. Due to these issues, from the Highfield sample onward, only total pyroxene is reported on the PDS and CheMin websites. For these later samples, the identification of augite, pigeonite, and orthopyroxene was derived from a detailed examination of the raw refinement outputs. This methodology allowed us to approximate the pyroxene phases despite the challenges in achieving precise fits due to overlapping peaks. Therefore, the results reported here should be considered a best estimate and not a definitive result, as reflected in the reported large uncertainties. While we cannot provide definitive results for pyroxene phases, these approximations can provide insight into the general compositional range and phases present in Gale crater, Mars.

3.3.1. Augite

Augite [$(Ca,Mg,Fe)_2Si_2O_6$; monoclinic, $C2/c$], frequently referred to as high-calcium pyroxene in planetary science, is a mineral commonly observed in mafic igneous rocks (e.g., basalt, gabbro) on Earth and in various planetary environments, including the Moon and Mars.

In this work, we report the composition of augite in samples analyzed by CheMin within Gale crater (14 of 40 CheMin samples; Table 6; Table S5 in Supplementary Materials contains a machine-readable version of unit-cell parameters, compositions, and associated uncertainties). We assume no additional chemical components outside of the Mg-Fe-Ca-Si-O system in our compositional estimates.

Table 6. Unit-cell parameters and estimated Mg, Ca, and Fe compositions of augite observed in Gale crater samples by the CheMin instrument. Uncertainty reported as 1σ. Machine-readable version of table available in Supplementary Materials (Table S5).

Augite Unit-Cell Parameters and Compositions							
Sample	***a* (Å)**	***b* (Å)**	***c* (Å)**	**β (°)**	**Mg (apfu)**	**Ca (apfu)**	**Fe (apfu)**
RK	9.77(3)	8.924(13)	5.263(11)	106.5(3)	0.94(9)	0.72(4)	0.34(10)
WJ	9.744(9)	8.925(11)	5.258(10)	106.36(6)	1.03(7)	0.75(4)	0.21(9)
GB	9.785(15)	8.922(13)	5.276(13)	106.45(9)	0.89(8)	0.73(3)	0.38(9)
OG	9.73(5)	8.91(3)	5.268(12)	106.8(4)	1.27(19)	0.66(7)	0.1(3)
DU	9.698(13)	9.00(3)	5.25(4)	105.75(19)	0.57(12)	0.77(5)	0.66(16)
ST	9.63(8)	9.01(4)	5.236(10)	105.81(16)	0.7(3)	0.74(8)	0.6(4)
RH	9.74(3)	9.005(4)	5.239(8)	105.53(15)	0.41(6)	0.81(4)	0.78(7)
GR	9.66(16)	9.00(9)	5.24(5)	105.5(12)	0.8(6)	0.9(3)	0.4(8)
NT	9.58(16)	9.02(13)	5.22(6)	105.4(3)	1.0(8)	1.0(3)	0(1)
PT	9.73(7)	8.98(6)	5.25(6)	106.1(4)	0.6(3)	0.72(9)	0.7(4)
MG	9.81(9)	8.9(1)	5.23(5)	106.1(4)	0.9(4)	0.89(15)	0.2(5)
ZE	9.69(5)	9.0(1)	5.25(5)	106.0(5)	1.1(6)	1.0(3)	−0.1(9)
CA	9.79(8)	8.90(8)	5.25(3)	106.3(7)	1.0(4)	0.82(13)	0.1(5)
TC	9.742(10)	8.939(16)	5.272(4)	106.3(2)	0.92(9)	0.76(5)	0.32(12)

3.3.2. Pigeonite

Pigeonite [$(Mg,Fe,Ca)_2Si_2O_6$; monoclinic, $P2_1/c$], colloquially known as low-calcium clinopyroxene, is another significant phase observed in planetary environments, including the Moon and Mars [85–87]. Pigeonite is chemically and structurally intermediate between *C2/c* augite (above) and *Pbca* orthopyroxene (below) [88].

In this work, we report the composition of pigeonite in samples analyzed by CheMin within Gale crater (26 of 40 CheMin samples; Table 7; Table S6 in Supplementary Materials contains a machine-readable version of unit-cell parameters, compositions, and associated uncertainties). We assume no additional chemical components outside of the Mg-Fe-Ca system in our compositional estimates.

Table 7. Unit-cell parameters and estimated Mg, Ca, and Fe compositions of pigeonite observed in Gale crater samples by the CheMin instrument. Uncertainty reported as 1σ. Machine-readable version of table available in Supplementary Materials (Table S6).

Pigeonite Unit-Cell Parameters and Compositions							
Sample	***a* (Å)**	***b* (Å)**	***c* (Å)**	**β (°)**	**Mg (apfu)**	**Ca (apfu)**	**Fe (apfu)**
RK	9.651(15)	8.942(18)	5.24(3)	108.35(18)	0.97(8)	0.00(3)	1.03(9)
JK	9.69(2)	8.917(18)	5.208(19)	108.57(14)	1.17(10)	0.19(6)	0.64(14)
CB	9.680(19)	8.93(2)	5.22(3)	108.53(10)	1.08(11)	0.14(8)	0.78(16)
WJ	9.648(16)	8.90(3)	5.210(16)	108.6(3)	1.29(13)	0.01(6)	0.70(15)
CH	9.651(16)	8.92(3)	5.210(16)	108.57(9)	1.10(9)	0.00(4)	0.90(9)
MJ2	9.67(3)	8.92(4)	5.20(4)	108.7(4)	1.14(16)	0.08(10)	0.8(3)
TP	9.67(4)	8.93(6)	5.19(4)	108.6(3)	1.1(3)	0.06(13)	0.9(3)
BS	9.672(9)	8.886(10)	5.222(9)	108.56(4)	1.44(7)	0.17(4)	0.40(9)
GB	9.68(2)	8.94(3)	5.25(3)	108.69(14)	0.94(12)	0.06(8)	1.00(17)
LB	9.67(3)	8.890(3)	5.21(3)	108.28(14)	1.54(17)	0.28(6)	0.18(17)
OK	9.667(7)	8.891(8)	5.217(8)	108.51(3)	1.39(7)	0.13(5)	0.48(10)
OG	9.68(4)	8.91(5)	5.25(4)	108.6(3)	1.2(3)	0.15(11)	0.6(3)
EB	9.63(3)	8.93(7)	5.17(3)	108.3(5)	1.2(3)	0.00(3)	0.9(3)
HU	9.68(4)	8.88(9)	5.189(18)	108.5(3)	1.5(5)	0.24(12)	0.3(6)
GG	9.61(7)	8.87(7)	5.26(8)	108.4(4)	1.6(3)	0.00(14)	0.4(4)

Table 7. *Cont.*

Pigeonite Unit-Cell Parameters and Compositions							
Sample	***a* (Å)**	***b* (Å)**	***c* (Å)**	**β (°)**	**Mg (apfu)**	**Ca (apfu)**	**Fe (apfu)**
MA	9.633(16)	8.90(3)	5.206(13)	108.30(11)	1.29(10)	0.00(3)	0.71(10)
MA3	9.62(5)	8.92(4)	5.211(12)	108.5(3)	1.18(14)	0.00(4)	0.82(14)
GR	9.591(8)	8.99(3)	5.16(4)	107.89(13)	0.79(11)	0.00(3)	1.21(12)
NT	9.610(19)	8.95(3)	5.209(19)	107.77(17)	1.03(14)	0.0(3)	1.0(4)
BD	9.62(3)	8.98(3)	5.20(3)	108.08(15)	0.80(10)	0.00(3)	1.20(10)
PT	9.69(4)	8.82(4)	5.24(4)	109.16(18)	1.75(14)	0.15(4)	0.10(13)
MG	9.73(5)	8.83(4)	5.27(5)	109.0(3)	1.62(16)	0.23(5)	0.15(14)
ZE	9.68(5)	8.92(6)	5.223(19)	108.5(3)	1.2(3)	0.17(13)	0.6(4)
AV	9.70(3)	8.90(3)	5.262(7)	109.01(10)	1.26(12)	0.19(4)	0.54(13)
CA	9.70(5)	8.84(5)	5.25(3)	109.3(5)	1.55(18)	0.16(5)	0.29(17)
TC	9.70(7)	8.91(5)	5.25(4)	108.5(3)	1.2(3)	0.29(9)	0.5(3)

3.3.3. Orthopyroxene Group

Enstatite ($Mg_2Si_2O_6$; orthorhombic, *Pbca*) and ferrosilite ($Fe_2Si_2O_6$; orthorhombic, *Pbca*), the two most common orthopyroxene group species, form a complete solid solution series. Any phase along this solid solution series is commonly referred to in Earth and planetary science as orthopyroxene [$(Mg,Fe^{2+}{}_2)Si_2O_6$]. Orthopyroxene is often a component of igneous rocks and has been identified in several planetary materials, including those of the Moon, Mars, and various meteorites.

In this work, we report the composition of orthopyroxene in samples analyzed by CheMin within Gale crater (18 of 40 CheMin samples; Table 8; Table S7 in Supplementary Materials contains a machine-readable version of unit-cell parameters, compositions, and associated uncertainties). We assume no additional chemical components outside of the Mg-Fe-Ca-Si-O system in our compositional estimates.

Table 8. Unit-cell parameters and estimated Mg, Ca, and Fe compositions of orthopyroxene observed in Gale crater samples by the CheMin instrument. Uncertainty reported as 1σ. Machine-readable version of table available in Supplementary Materials (Table S7).

Orthopyroxene Unit-Cell Parameters and Composition			
Sample	**Mg (apfu)**	**Ca (apfu)**	**Fe (apfu)**
JK	0.75(8)	0.00(4)	1.25(8)
CB	0.83(8)	0.02(5)	1.16(10)
BS	0.69(7)	0.00(2)	1.31(7)
GH	0.80(8)	0.04(4)	1.16(9)
LB	0.81(10)	0.00(6)	1.19(11)
OK	0.9(2)	0.00(6)	1.1(2)
OU	0.81(11)	0.01(6)	1.19(12)
DU	1.3(3)	0.08(2)	0.6(3)
ST	0.73(5)	0.00(2)	1.27(5)
RH	1.5(3)	0.08(2)	0.4(4)
HF	0.99(12)	0.08(2)	0.93(12)
GR	1.24(15)	0.01(5)	0.75(16)
BD	1.15(8)	0.00(3)	0.85(8)
PT	1.15(10)	0.08(2)	0.77(10)
MG	1.0(3)	0.08(2)	1.0(3)
ZE	1.28(9)	0.08(2)	0.64(9)
AV	1.5(2)	0.08(2)	0.4(3)
CA	1.0(3)	0.01(5)	1.0(3)

The mean composition of Gale crater pyroxene is similar to that of martian meteorites [73–77], although there are some differences in their compositional ranges (Figure 7). There are 2556 meteorite pyroxene samples plotted on the graph in Figure 7, along with 58

samples from Gale crater (14 augite, 26 pigeonite, 18 orthopyroxene). In the martian meteorite dataset, there are 834 "high-Ca pyroxene" samples, where Ca/(Ca+Fe+Mg) $\geq$ 0.20, and 1722 "low-Ca pyroxene" samples [Ca/(Ca+Fe+Mg) < 0.20]. In the Gale crater dataset, there are 14 "high-Ca pyroxene" samples and 44 "low-Ca pyroxene" samples. The mean composition of martian meteorite pyroxene is $[Mg_{0.54(13)}Fe_{0.30(10)}Ca_{0.17(14)}]_2Si_2O_6$. The mean Gale crater pyroxene composition is $[Mg_{0.54(14)}Fe_{0.33(18)}Ca_{0.13(16)}]_2Si_2O_6$). The mean composition of "high-Ca pyroxene" in martian meteorites is $[Mg_{0.41(8)}Fe_{0.23(8)}Ca_{0.36(6)}]_2Si_2O_6$, and the mean of "low-Ca pyroxene" is $[Mg_{0.60(33)}Fe_{0.33(9)}Ca_{0.07(4)}]_2Si_2O_6$. The mole fractions of Fe, Mg, and Ca in martian meteorites are in the ranges of 0.07–0.79, 0.07–0.83, and 0.00–0.50, respectively. The mole fractions of Fe, Mg, and Ca in the Gale crater samples range from −0.07 (Zechstein) to 0.66 (Big Sky), 0.21 (Rockhall) to 0.88 (Pontours), and 0.00 (several pigeonite and orthopyroxene samples) to 0.50 (Zechstein), respectively. Note that Zechstein augite has a negative estimated value of Fe; given that the uncertainties in unit-cell parameters are no greater than average, it is likely that Zechstein contains appreciable amounts of one or more other elements not accounted for with these algorithms (see Discussion). The "high-Ca pyroxene" mole fractions in martian meteorites are in the ranges of Fe = 0.07–0.66 and Mg = 0.10–0.59, whereas those of "low-Ca pyroxene" are in the ranges of Fe = 0.16–0.79 and Mg = 0.07–0.83.

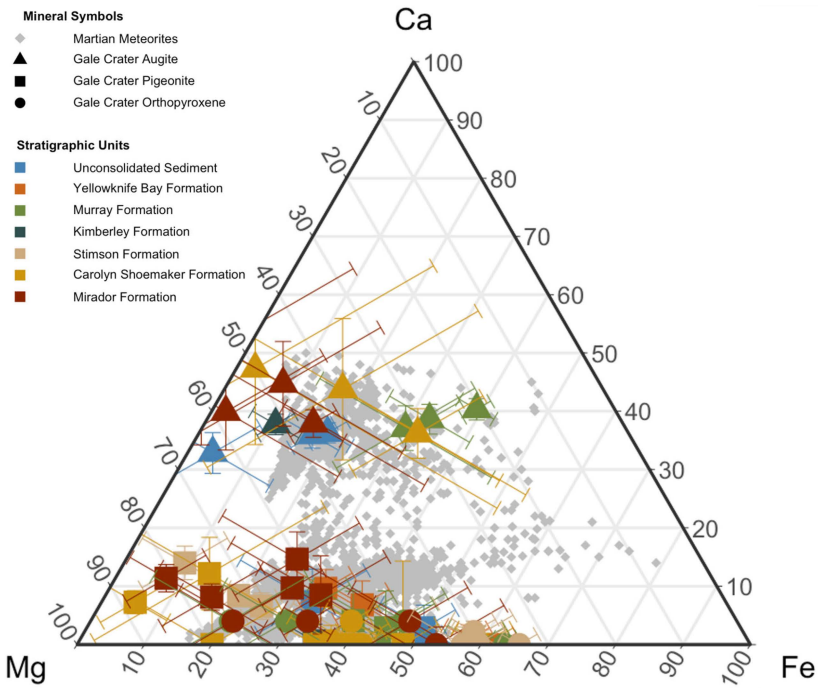

Figure 7. Pyroxene sample composition as a function of Ca (%), Mg (%), and Fe (%) in martian meteorites and Gale crater samples analyzed by CheMin. Gale crater sample error bars are at 1σ uncertainty.

While the mean composition of martian meteorite and Gale crater pyroxene are similar, distinct compositional domains are occupied by each suite of samples. Specifically, there are several martian meteorite pyroxene samples that have higher Fe content than any samples analyzed in Gale crater. In contrast, there are several Gale crater pigeonite and augite samples with higher Mg content than any of the martian meteorites, as much as 0.11 mole fraction Mg more than the highest abundance of Mg in a martian meteorite. Additionally, martian meteorite pyroxene has many samples with compositions intermediate between the augite and pigeonite + orthopyroxene compositions of Gale crater. This is likely due to two reasons: (1) the intermediate compositions observed in martian meteorites are the result of microprobe measurements performed on sample regions of augite and pigeonite exsolution lamellae, resulting in the analysis of the composition of two crystallographically distinct phases as one; (2) the microprobe can analyze the fine-scale zonation in pyroxene

grains, capturing compositions of very small regions of more intermediate compositions. In contrast, XRD provides an average of the total sample volume, potentially obscuring the distinct intermediate phases of low abundance and resulting in a summed pattern.

3.4. Cubic Spinel Oxide Group Minerals

There are 30 IMA-recognized cubic spinel oxide minerals (rruff.info/ima; date accessed: 23 January 2024). Cubic spinel oxide group minerals have a general chemical formula of AB_2O_4 and exhibit a cubic crystal structure. The A site is generally tetrahedral and accommodates 3+ cations, with 4+ and, rarely, 5+ cations substituting in this site. The slightly larger, octahedral *B* site usually accommodates 2+ cations, with rare substitution of 3+ or 4+ cations and/or site vacancies (□). The cubic spinel oxide structure is known to accommodate many transition elements (Fe^{2+}, Fe^{3+}, Ti^{4+}, Cr^{3+}, Mn^{2+}, Mn^{3+}, Co^{2+}, Co^{3+}, Cu^{2+}, Zn^{2+}, V^{2+}, V^{3+}, and Ni^{2+}) and site vacancies as well as metals, metalloids, and non-metals (i.e., Mg^{2+}, Ca^{2+}, Si^{4+}, Al^{3+}, Ge^{4+}, Sb^{5+}). On Earth, spinel oxides are ubiquitous, with magnetite ($Fe^{2+}Fe^{3+}{}_2O_4$), chromite ($Fe^{2+}Cr^{3+}{}_2O_4$), and spinel ($MgAl_2O_4$) being among the most common and ringwoodite (Mg_2SiO_4) being an important component of Earth's mantle. On Mars and in martian meteorites, magnetite, chromite, maghemite [$(Fe^{3+}{}_{0.67}\square_{0.33})Fe^{3+}{}_2O_4$], and ulvöspinel ($Fe^{2+}{}_2Ti^{4+}O_4$), commonly referred to as titanomagnetite, have been frequently detected. A detailed examination of spinel oxide composition and the distribution of elements in martian meteorites can be found in the work of Morrison et al. (2018a) [8]. Spinel oxides form in a wide range of environments, from igneous and hydrothermal processes to secondary alteration and microbial mediation [54,55,89]. The composition of the spinel oxide phase provides information about which of these varied conditions were most likely to have produced the specimen in question. Therefore, it is critical that we attempt to narrow the possible spinel oxide compositions present in the Gale crater samples analyzed by CheMin. However, the cubic nature of the spinel crystal structure provides only one unit-cell parameter, the *a* cell edge, and therefore, we are limited to providing a list of possible chemical systems and the estimated composition should the sample be limited to that system (see Figure 8).

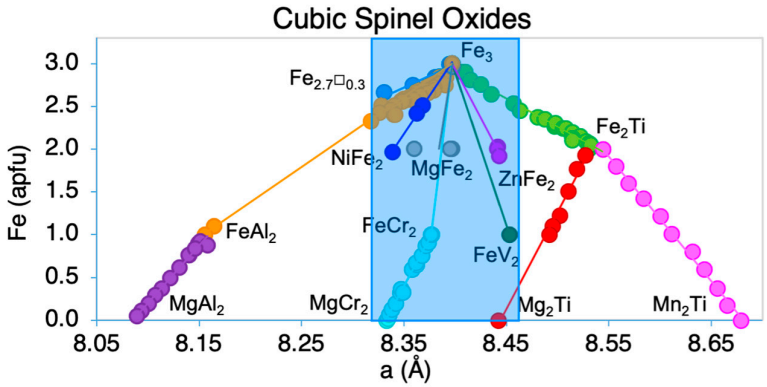

Figure 8. Select spinel oxide phases (M_3O_4) as a function of Fe content and *a* unit-cell parameter. The blue region represents the range of Gale crater spinel oxide *a* unit-cell parameters. Purple circles represent the $MgAl_2O_4$-$FeAl_2O_4$ solid solution series, orange circles represent $FeAl_2O_4$-Fe_3O_4, light blue circles represent $Fe_{2.7}\square_{0.03}$-Fe_3O_4, dark blue circles represent $NiFe_2O_4$-Fe_3O_4, grey circles represent $MgFe_2O_4$-Fe_3O_4, cyan circles represent $FeCr_2O_4$-$MgCr_2O_4$, dark green circles represent FeV_2O_4-Fe_3O_4, light purple circles represent $ZnFe_2O_4$-Fe_3O_4, light green circles represent $TiFe_2O_4$-Fe_3O_4, red circles represent $TiFe_2O_4$-$TiMg_2O_4$, and pink circles represent $TiFe_2O_4$-$TiMn_2O_4$ solid solution series.

In this work, we report the composition of cubic spinel oxides in samples analyzed by CheMin within Gale crater (19 of 40 CheMin samples; Table 9; Table S8 in Supplementary Materials contains a machine-readable version of unit-cell parameters, compositions, and associated uncertainties). An estimated composition is reported for each plausible two- and three-component system, assuming no additional components outside of those stated

in the chemical formula. Estimated compositions are omitted for unit-cell parameters that fall outside the plausible range for a given phase, resulting in implausible or impossible chemical compositions. Note that these values provide a good estimate of the bulk composition of the spinel oxide phases, but it is likely that there are other minor components not accounted for in the reported compositions.

Based on the compositional estimates, it is plausible that the cubic spinel oxide phases in Gale crater contain some combination of Fe, site vacancies, Ni, Al, Mg, and/or Cr, with the possibility of up to 0.01–0.02 Ti (apfu) (Table 9, Figure 8). Among the possible compositional estimates, Fe content ranges from 0.51 apfu [assuming (Fe,Mg,Cr); Telegraph Peak] to 2.99 apfu (assuming (Fe,Ti) system; Big Sky), with a mean Fe content of 2.44(75) apfu. If we assume a Fe- and site-vacancy-only composition, the mean Gale crater cubic spinel oxide is magnetite with a Fe content of 2.81(8) apfu [$Fe_{2.81(8)}\square_{0.19(8)}O_4$]. If we assume a composition in the $FeAl_2O_4$ system, the mean Gale crater cubic spinel oxide is magnetite with a mean composition of $Fe_{2.78(15)}Al_{0.22(15)}O_4$. If we assume that only Ni substitutes for Fe, the mean Gale crater composition is $Fe_{2.59(21)}Ni_{0.41(21)}O_4$. If we assume the samples exist in the $Fe_{1-x}Al_{2-y}\square_{x+y}O_4$ chemical space, the mean Gale composition is $Fe_{2.69(12)}Al_{0.15(7)}\square_{0.16(6)}O_4$. Twelve of the seventeen CheMin samples had unit-cell parameters that could possibly correspond to a cubic spinel oxide composition in the Fe-Mg-Cr system; the mean composition of those twelve CheMin samples is $Cr_{2.00(5)}Fe_{0.81(21)}Mg_{0.19(21)}O_4$. Three CheMin samples (Big Sky, Greenhorn, and Hutton) had unit-cell parameters that indicate the possibility of a composition in the Fe-Mg solid solution; the mean composition of these samples, assuming Fe-Mg only, is $Fe_{2.37(16)}Mg_{0.63(16)}O_4$. Two samples had unit-cell parameters that indicated the possibility of containing Ti, specifically the solid solution between Fe and Ti; assuming Fe and Ti only, the Big Sky sample has an estimated composition of $Fe_{2.99(3)}Ti_{0.01(3)}O_4$, and the Hutton sample has a composition of $Fe_{2.98(3)}Ti_{0.02(3)}O_4$.

Table 9. Unit-cell parameters and estimated chemical compositions, as cation apfu, of cubic spinel oxides observed in Gale crater samples by the CheMin instrument. Estimated compositions are omitted ("--") for unit-cell parameters that fall outside the plausible range for a given phase. Uncertainty reported as 1σ. Machine-readable version of table available in Supplementary Materials (Table S8).

Cubic Spinel Oxide Unit-Cell Parameters and Compositions																		
	Source	**RK**	**JK**	**CB**	**WJ**	**CH**	**MJ2**	**TP**	**BK**	**BS**	**GH**	**GB**	**LB**	**OK**	**OG**	**ST**	**EB**	**HU**
	a (Å)	8.381(4)	8.372(2)	8.369(2)	8.373(1)	8.365(3)	8.357(2)	8.355(1)	8.359(1)	8.389(1)	8.387(1)	8.380(8)	8.380(3)	8.383	8.370(17)	8.313(14)	8.362(3)	8.391(1)
$Fe_{3-x}\square_xO_4$	Fe (apfu)	2.86(5)	2.82 (5)	2.81(5)	2.83(5)	2.79(5)	2.76(5)	2.75(5)	2.77(5)	2.90(5)	2.89(5)	2.86(6)	2.86(5)	2.87(5)	2.81(9)	2.57(8)	2.78(5)	2.91(5)
$MgFe_2O_4$	Fe (apfu)	--	--	--	--	--	--	--	--	2.37(9)	2.22(9)	--	--	--	--	--	--	2.52(12)
	Mg (apfu)	--	--	--	--	--	--	--	--	0.63(9)	0.78(9)	--	--	--	--	--	--	0.48(12)
Fe_2TiO_4	Fe (apfu)	--	--	--	--	--	--	--	--	2.99(3)	--	--	--	--	--	--	--	2.98(3)
	Ti (apfu)	--	--	--	--	--	--	--	--	0.01(3)	--	--	--	--	--	--	--	0.02(3)
$FeAl_2O_4$	Fe (apfu)	2.87(4)	2.79(3)	2.77(3)	2.80(2)	2.74(3)	2.67(3)	2.65(2)	2.69(2)	2.93(2)	2.92(2)	2.86(7)	2.86(3)	2.89(2)	2.78(14)	2.31(12)	2.71(3)	2.95(2)
	Al (apfu)	0.13(4)	0.21(3)	0.23(3)	0.20	0.26(3)	0.33(3)	0.35(2)	0.31(2)	0.07(2)	0.08(2)	0.14(2)	0.14(3)	0.11(2)	0.22(14)	0.69(12)	0.29(3)	0.05(2)
$NiFe_2O_4$	Fe (apfu)	2.73(4)	2.57(3)	2.52(3)	2.59(2)	2.44(3)	2.03(3)	2.27(2)	2.34(2)	2.87(2)	2.84(2)	2.71(7)	2.71(3)	2.76(2)	2.53(14)	--	2.38(3)	2.91(2)
	Ni (apfu)	0.27(4)	0.43(3)	0.48(3)	0.41(2)	0.56(3)	0.70(3)	0.73(2)	0.66(2)	0.13(2)	0.16(2)	0.29(7)	0.29(3)	0.24(2)	0.47(14)	--	0.62(3)	0.09(2)
$(FeMgCr^{3+})_3O_4$	Fe (apfu)	1.09(9)	0.89(5)	0.82(5)	0.91(3)	0.73(7)	0.55(5)	0.51(3)	0.60(3)	--	--	1.07(18)	1.07(7)	--	0.84(38)	--	0.66(7)	--
	Mg (apfu)	−0.09(9)	0.11(5)	0.18(5)	0.09(3)	0.27(7)	0.45(5)	0.49(3)	0.40(3)	--	--	−0.07(18)	−0.07(7)	--	0.16(38)	--	0.34(7)	--
	Cr (apfu)	2.00(13)	2.00(7)	2.00(7)	2.00(5)	2.00(10)	2.00(7)	2.00(5)	2.00(5)	--	--	2.00(26)	2.00(10)	--	2.00(54)	--	2.00(10)	--
$Fe_{1-x}Al_{2-y}\square_{x+y}O_4$	Fe (apfu)	2.76(5)	2.71(4)	2.69(4)	2.71(4)	2.66(5)	2.61(4)	2.60(4)	2.62(4)	2.82(4)	2.80(4)	2.76(7)	2.76(5)	2.78(4)	2.69(12)	2.32(10)	2.64(5)	2.83(4)
	Al (apfu)	0.11(6)	0.14(6)	0.15(6)	0.14(6)	0.16(6)	0.19(6)	0.20(6)	0.19(6)	0.08(6)	0.08(6)	0.11(7)	0.11(6)	0.10(6)	0.15(9)	0.36(8)	0.18(6)	0.07(6)
	Vac (□pfu)	0.13(8)	0.16(7)	0.16(7)	0.15(7)	0.18(8)	0.20(7)	0.20(7)	0.19(7)	0.11(7)	0.11(7)	0.13(9)	0.13(8)	0.12(7)	0.16(15)	0.32(13)	0.18(8)	0.10(7)

Figure 9 explores the composition and elemental distribution of major elements measured in 531 samples of spinel oxide from martian meteorites [74,75,90–131]. Martian meteorites have a mean Fe content of 1.77(73) apfu, with a range of 0.62–2.97 apfu; Mg has a mean of 0.11(10) apfu and a range of 0.00–0.43 apfu and was observed in 530 of the samples; Al has a mean of 0.18(13) apfu with a range of 0.001–1.01 apfu; Cr has a mean of 0.64(65) apfu and a range of 0.00–1.70 apfu and was found in 494 samples; and Ti has a mean of 0.27(25) apfu with a range of 0.003–0.95 apfu. In addition to the elements present in major abundance, there are several other minor elements found in various samples of the martian meteorite spinel. Manganese was found in 517 samples, with a maximum abundance of 0.045 apfu; Si was detected in 345 of the samples, with a maximum of 0.051 apfu; 333 samples were found to have V, at a maximum value of 0.054 apfu; Ca was observed in 216 samples, with a maximum abundance of 0.020 apfu; 107 samples contain Ni, with a maximum abundance of 0.012 apfu; Co was detected in 71 samples, with a maximum of 0.007 apfu. Zinc was found in 59 of the samples, with a maximum abundance of 0.008 apfu; 17 samples contained K (maximum = 0.001 apfu); 13 samples contained Na (maximum = 0.014 apfu); and 9 samples contained P (maximum 0.004 apfu).

It is plausible, based on the unit-cell parameters, that the composition of the spinel oxide analyzed in Gale crater is similar to that of martian meteorites. The notable exception is Ti, which is not plausible based on the calculations of the two- and three-element systems explored herein. However, it is probable that the composition of the Gale crater samples is more complex than 2–3 chemical elements, in which case some minor amount of Ti could be present in the sample.

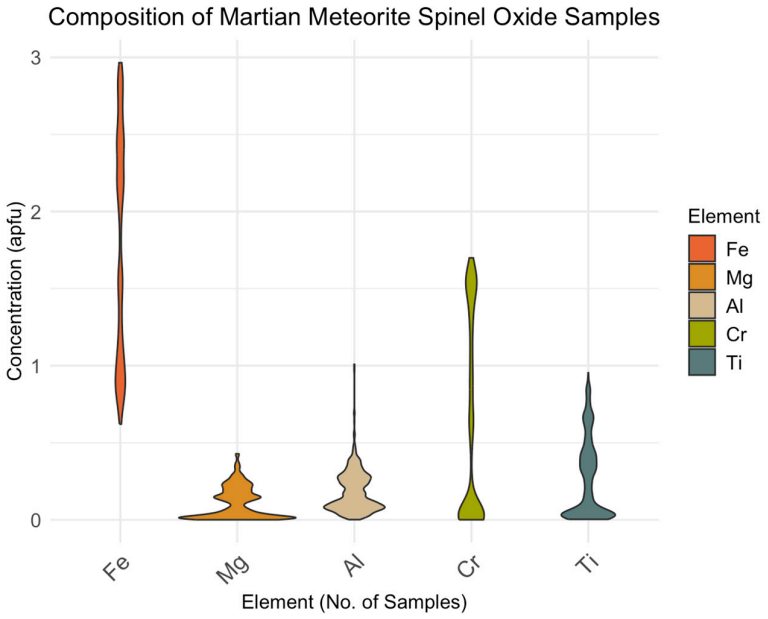

Figure 9. Violin plot of martian meteorite spinel oxide elemental concentrations (apfu) distributions. Each violin represents the distribution of major elements (Fe, Mg, Al, Cr, and Ti) across the 531 sampled meteorites. The width of each violin indicates the density of data points.

If we assume a composition along the magnetite ($Fe^{2+}Fe^{3+}{}_2O_4$)–maghemite [$(Fe^{3+}{}_{0.67}\square_{0.33})Fe^{3+}{}_2O_4$] solid solution, the cubic spinel oxide measured with CheMin in the fluviolacustrine and cemented eolian rock samples of Gale crater, Mars, has a mean composition of $Fe_{2.81(8)}\square_{0.19(8)}O_4$ (Table 9; Figure 10). The range of composition is Fe (apfu) = 2.57(8) (Stoer) to Fe = 2.91(5) (Hutton). The Yellowknife Bay Formation samples have a mean magnetite composition of 2.82(4) Fe (apfu) and a range of 2.81(5) Fe (Cumberland) to 2.82(5) Fe (John Klein). The Pahrump Hills unit of the Murray Formation contains a cubic spinel oxide phase throughout the section; its mean magnetite composition is 2.77(3) Fe

(apfu) with a range of 2.71(5) Fe (Telegraph Peak) to 2.79(5) Fe (Confidence Hills). One other Murray Formation sample, Stoer of the Pettegrove Point Member, contains a cubic spinel oxide, albeit in relatively low abundance (0.7 wt. % of the crystalline material). The Stoer magnetite composition is 2.57(8) Fe (apfu), significantly lower than that of the other Murray Formation (Pahrump Hills) samples and lower still than the other Gale crater samples. The Stimson Formation samples each contain a cubic spinel oxide phase, with a mean magnetite composition of 2.86(5) Fe (apfu). The composition in the Stimson Formation ranges from Fe (apfu) = 2.78(5) (Edinburgh) to 2.90(5) (Big Sky). Only one sample of the upper stratigraphic units contains appreciable magnetite—the Hutton sample of the Carolyn Shoemaker Formation with a magnetite composition of 2.91(5) Fe (apfu).

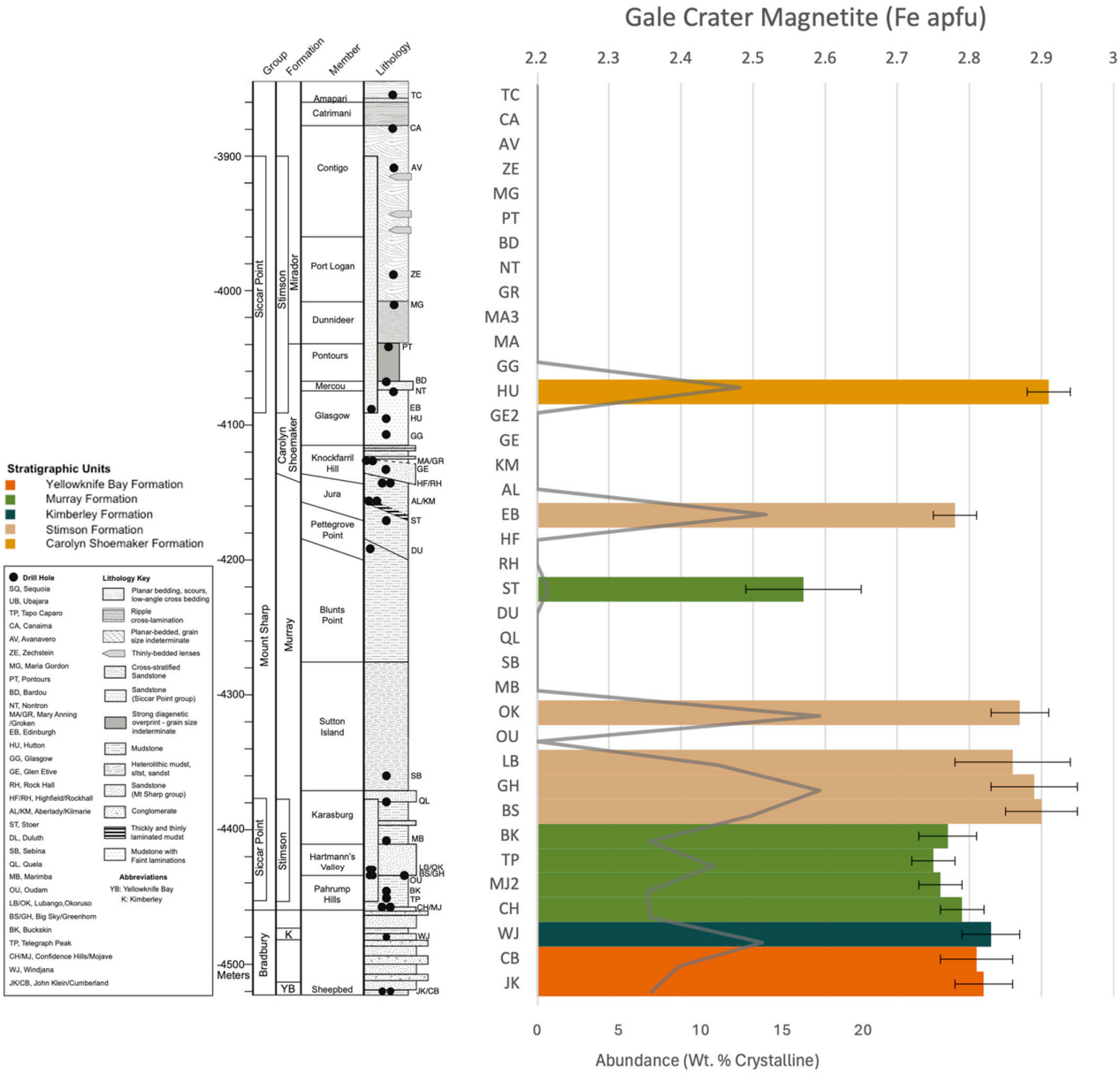

Figure 10. Cubic spinel oxide composition as magnetite–maghemite (Fe apfu solid solution with site vacancy) of the fluviolacustrine and cemented eolian samples analyzed by the CheMin instrument along the Gale crater stratigraphic section. Error bars represent uncertainty to 1σ. Spinel oxide abundance as wt. % of the crystalline sample fraction is displayed as a gray line.

4. Discussion

4.1. Plagioclase

The comprehensive analysis of plagioclase compositions in Gale crater fluviolacustrine and eolian samples offers a window into the crystallization history and environmental conditions on Mars during the formation of these minerals. The dominance of intermediate to high anorthite content (An14 to An59) is indicative of a Ca-rich parental material, likely basaltic to andesitic in nature. The variability in plagioclase composition throughout the Gale crater stratigraphy signals a dynamic geological setting, possibly characterized by fluctuations in temperature, pressure, the availability of Ca and Na, and fractional crystallization [54,62]. The relatively higher anorthite content in the Aberlady sample (An59) may point to crystallization from a more Ca-rich melt or under conditions where Ca was more readily incorporated into the plagioclase crystal lattice, such as at higher pressures or temperatures. Contrastingly, the lower anorthite content in the Edinburgh sample (An24) could reflect crystallization from a more Na-rich or Ca-depleted source, or at conditions favoring lower temperatures. The mean composition of An40 for Gale crater plagioclases aligns closely with the mean martian meteorite plagioclase composition (An44), suggesting that the petrogenetic processes responsible for the formation of plagioclase at Gale crater are broadly representative of those at work elsewhere on Mars. This could imply a degree of homogeneity in the martian crust's composition or at least in the environments where these samples originated.

The plagioclase composition in Gale crater samples, derived from CheMin data, indicates a Mars that has experienced a complex history of magmatic processes, with the resultant plagioclase compositions recording changes in pressure, temperature, and magma composition during crystallization.

4.2. Alkali Feldspar Group Minerals

The data from CheMin samples offer insights into the crystallization environment of alkali feldspar minerals, reflecting the thermal and geochemical history of the martian crust in Gale crater. The CheMin data show a compositional range in Gale crater alkali feldspars from Ab0 to Ab70, with a mean composition of Ab28. The presence of highly disordered sanidine indicates that some of the alkali feldspar samples formed in high-temperature volcanic settings, likely from rapidly cooling lava flows or tephra deposits [54,62]. In situ precipitation of disordered alkali feldspar at the Windjana location resulting from hydrothermal fluid interactions with plagioclase feldspar could also be possible [16]. However, the data also suggest a range of cooling rates, given the variation in the degree of ordering observed in some of the samples. While most of the samples are fully disordered or only slightly ordered, there are a few samples (i.e., Glen Etive, Glen Etive 2) that display higher degrees of ordering. This ordering could be due to a slower initial crystallization in an igneous or hydrothermal setting or could be due to post-crystallization thermal processes that led to annealing. The compositions and ordering of the alkali feldspar in Gale crater point to a parent body that was K-rich, possibly Na-depleted. The absence of alkali feldspar compositions with Ab > 80 indicates a lack of sodium-rich environments in the Gale crater crustal history sampled by the CheMin instrument. The mean composition of Gale crater samples is significantly lower in Na than that of martian meteorites (Ab90). This may indicate that the Gale crater site is a distinct crustal component of Mars, not widely represented in the meteorite samples. This finding is significant as it could point to local geological processes that may not be global in nature on Mars, such as localized magma differentiation or alteration phenomena, and can provide constraints to models of the martian crust, suggesting that the conditions necessary to form Na-rich feldspars either did not exist or are not preserved in the regions sampled by CheMin.

The alkali feldspar results from Gale crater provide a nuanced picture of the martian crust's thermal and geochemical history. The presence of potassium-rich feldspar and the degree of ordering demonstrate a complex interplay of crystallization, cooling rates, and

possibly subsequent thermal alteration. Comparisons with martian meteorites highlight the diversity of martian crustal processes and underscore the importance of in situ analyses for understanding the geologic history of Mars.

4.3. Olivine Group Minerals

The presence of olivine (i.e., forsterite) in Gale crater is indicative of the primary magmatic processes that have taken place on Mars. The composition of the olivine provides insight into the mantle composition, degree of partial melting and fractionation, and cooling history of the martian crust [54,62,132–134]. The intermediate to high values of Mg content in the Gale crater olivine (Fo54–Fo72) indicate a relatively Mg-rich parent body, possibly a relatively high-temperature magmatic source that did not experience significant Fe-enrichment through fractional crystallization or alteration. This suggests that Gale crater olivine crystallized relatively early, capturing the composition of the early mantle or early differentiation of basaltic crust. The comparison of martian meteorites further supports the conclusion that Gale olivine is from a primitive, relatively undifferentiated source. Gale olivine shows a similar composition to that of shergottites, which are thought to form through the rapid cooling of primitive, mantle-derived basalts. In contrast, nakhlites tend to have higher Fe content and are thought to form through slower cooling of relatively evolved magmas that have undergone extensive differentiation. Additionally, given the extensive history of aqueous alteration and olivine's instability under such conditions (i.e., generally resulting in serpentinization [135]), it is noteworthy that olivine can still be found in several of the sedimentary rock layers. It is likely, given the sedimentary nature of these rocks, that the materials were sourced from several distinct areas that underwent varying degrees of alteration prior to consolidation and cementation into their current strata. In addition to providing information about the alteration experienced by the original source rock, it is also likely that the presence of olivine in a Gale crater stratigraphic unit is an indicator of a restricted amount of post-lithification alteration.

The olivine composition observed in Gale crater provides insight into the early mantle and crust on Mars. They underscore a history of a planet with a mantle composition and thermal evolution that has fostered the preservation of early magmatic products, offering a window into the formative years of martian geology and its subsequent evolution.

4.4. Pyroxene Group Minerals

The presence of augite, pigeonite, and/or orthopyroxene in 32 out of 40 samples underscores the importance of pyroxenes as markers of petrologic processes on Mars. Despite the large error bars in the compositional estimates, these preliminary findings allow us to make some broad inferences about the petrology of the samples, including the conditions of temperature, pressure, and depth of formation, as well as insights into the protolith from which these minerals crystallized. The variety of pyroxene compositions, from Fe-rich to Mg-dominant, suggests a range of igneous processes have shaped the rocks in Gale crater [54,62]. The occurrence of pigeonite and augite points to a history of magmatic activity, possibly from basaltic flows or intrusions, where relatively high temperatures were prevalent during the crystallization processes. Pigeonite and orthopyroxene are often found in tholeiitic basalt, a relatively silica-rich, evolved mafic rock commonly observed on Earth at mid-ocean ridges (MORB) and on the moon in the lunar maria [136]. The occurrence of orthopyroxene may indicate either crystallization from a high magnesium basaltic lava or a subsequent thermal metamorphism that could have affected the primary minerals. The diversity in pyroxene phase and chemistry can be indicative of varying cooling rates and/or a range in the degree of partial melting or fractional crystallization, and therefore the potential for multiple generations of igneous activity.

Note that while the mean compositions of martian meteorite and Gale crater pyroxene are similar, distinct compositional domains are occupied by each suite of samples. There are several Gale crater pigeonite and augite samples with higher Mg content than any of the known martian meteorites, as much as 0.11 mole fraction Mg more than the most

Mg-rich clinopyroxene in a martian meteorite. This suggests that martian meteorites do not represent all mineralogical and petrological domains present in Gale crater.

In summary, pyroxenes, including augite, pigeonite, and orthopyroxene found in martian sedimentary rock samples from Gale crater, suggest a complex history of high-temperature magmatic and volcanic processes and variable cooling rates, indicative of diverse igneous activity on Mars, and likely represent terrains not represented by the suite of martian meteorites studied on Earth.

4.5. Spinel Oxide Group Minerals

Oxide spinel minerals observed in sedimentary rocks were likely derived from igneous protoliths and may have many different origins. With the CheMin results in Gale crater, we can narrow the possible compositions present at this location on Mars, thereby providing some insight into the past mineralizing environments. It is reasonable to assume that in addition to Fe, there may also be some amount of site vacancies, Al, Cr, Ni, Mg, and/or Mn. Cation-deficient magnetite (i.e., magnetite with site vacancies) is an alteration product of olivine, resulting from diagenetic oxidation in a near-surface environment [9,21]. Given the likely igneous protolith, the known presence of olivine in some rock units, and the probable diagenesis that occurred post-deposition in a sedimentary basin, it is reasonable to expect this mode of mineralization. Aluminum and Mg, as a minor substituent in magnetite, as well as Cr, as a minor to major substituent in magnetite or as chromite, are common in basaltic rocks, with Cr possibly reflecting an ultramafic source. Nickel is rarely observed in martian meteorite spinels; on Earth, it is associated with spinel oxides from trace amounts to major, Ni-dominant phases, all of which are commonly associated with ultramafic igneous sources, and, to a lesser extent, hydrothermal mobilization [54]. While Ti is a common substituent in martian meteorite magnetite, the CheMin results support the presence of little to no Ti in the Gale crater spinel, which might be indicative of the local geology or the specific alteration processes the crater has undergone. It is possible for some minor amount to be present with complex substitution of smaller ionic radii elements, but it is clearly not present in high abundances.

These findings demonstrate the likelihood of multiple generations of spinel oxides in Gale crater, crystallizing from several distinct mineralizing processes, in particular extrusive mafic rock (basalt) and the diagenetic alteration thereof.

4.6. Future Work

In addition to the continued development of spacecraft X-ray diffraction instrumentation to increase speed, efficiency, and resolution [137–140] which are necessary to address the challenges associated with the extreme environmental conditions on Mercury and Venus, our future work will leverage advanced machine learning methods and a growing base of mineralogical information to extend the analysis of mineral XRD data to more complex and diverse mineral systems [141,142]. By refining predictive models for both major and minor elements, we aim to gain a deeper understanding of the geological histories across planetary bodies, with a particular focus on Mars. We will explore an array of minerals—including carbonates, phosphates, sulfates, halides, oxides, and silicates—and we will examine their mineralizing environments and paragenetic modes on Earth and in meteorites in order to characterize the formational conditions and alteration histories of the planetary bodies in our solar system [54,56–63]. These efforts will contribute to the development of next-generation mineralogical spacecraft instrumentation, enhancing the capabilities of X-ray diffraction analysis for future space missions and creating the most powerful mineralogical analysis technique in space exploration.

4.6.1. Expanding Chemical Complexity

Building on the foundation of the work presented herein, we will use machine learning methods and the wealth of mineral X-ray diffraction and chemical data to extend our investigations beyond the limited compositional ranges explored in this study. While

regression and optimization methods are suitable for estimating major elements in two- and three-component systems (e.g., Mg-Fe in olivine, Mg-Fe-Ca in pyroxene), machine learning frameworks (e.g., Label Distribution Learning [143]) employ advanced analytical methods (e.g., k-nearest neighbor, neural networks, Bayes classifiers, Support Vector Machines) capable of characterizing major and minor elements in mineral systems with many compositional components [141,142,144]. This work will include the following: (1) It will include the incorporation of major and minor elements naturally occurring in the mineral systems explored here and in the work of Morrison et al. (2018) [8,9]. (2) This work will be expanded to other planetary-relevant mineral systems (see Section 4.6.2 below) with an aim towards preparation for future spacecraft missions. (3) These crystal chemical methods will be extended to use site positions and occupancies in addition to unit-cell parameters, with a particular focus on cubic mineral systems, including garnet and spinel oxide. This approach will greatly expand our ability to make predictions in previously limited cubic mineral systems. (4) Our machine learning models will be refined to better handle the sparsity and size limitations characteristic of mineralogical data. This refinement will focus on algorithmic adjustments for enhanced data extrapolation and robustness in sparse data environments, thereby broadening the interpretive capabilities of XRD analysis in planetary missions, including MSL. (5) Alongside these technical developments, concerted efforts will be directed towards characterizing the relationships among mineral composition and their paragenetic modes, constructing a more comprehensive understanding of the geologic history of minerals on Earth and other planets in our solar system [54,55,145].

This approach enables the prediction of complex, multi-component compositions in a myriad of mineral systems from XRD data alone. Minor elements contain a wealth of information regarding their formational conditions and alteration histories (e.g., geothermometers, geobarometers, and indicators of fluid interactions, redox conditions, hydrothermalism, and metamorphism). Unlocking the geochemical nuances of martian mineralogy will allow us to interpret the geological history of Mars with greater precision, and these generalizable methods will allow us to expand these estimations throughout our solar system. The combination of mineralogical data, crystal chemical relationships, machine learning, and X-ray diffraction results in the most powerful mineralogical spacecraft instrumentation to date.

4.6.2. Expanding to Other Mineral Systems

The exploration of mineral systems on Mars and other planetary bodies presents numerous opportunities for advancing our understanding of planetary geology. For the CheMin instrument on Mars and potential instruments on future missions, we will explore other mineral systems and develop new crystal chemical algorithms for estimating the composition of all planetary-relevant mineral phases. These mineral systems include the following: Carbonates, such as those of the calcite structure {calcite [$Ca(CO_3)$], magnesite [$Mg(CO_3)$], and siderite [$Fe(CO_3)$]}, are important for understanding the aqueous, atmospheric, and habitability history of a planetary surface, including pH, temperature, and composition [55,64,65,146]. Phosphates, such as those of the apatite crystal structure {fluor-, chlor-, and hydroxyl-apatite [$Ca_5(PO_4)_3(F,Cl,OH)$]} and the cerite structure {merrillite [$Ca_9NaMg(PO_4)_7$], ferromerrillite [$Ca_9NaFe^{2+}(PO_4)_7$], whitlockite [$Ca_9Mg(PO_3OH)(PO_4)_6$]}, are key indicators of hydrothermal activity and can trap volatiles (e.g., F, Cl, and H). They are important for understanding water–rock interactions and have potential biological relevance due to the role of phosphorus in terrestrial life [55]. Additionally, phosphate minerals are crucial for studying the origin and evolution of KREEP, a component rich in K, rare earth elements, and P, which is a marker of extreme evolution from primordial lunar magma(s) and remains poorly understood yet widely distributed. Sulfates, such as those of the kieserite structure {kieserite [$Mg(SO_4)\cdot H_2O$] and szomolnokite [$Fe(SO_4)\cdot H_2O$]} and the starkeyite structure {starkeyite [$Mg(SO_4)\cdot 4H_2O$], rozenite, [$Fe^{2+}(SO_4)\cdot 4H_2O$], and ilesite [$Mn^{2+}(SO_4)\cdot 4H_2O$]}, and calcium sulfates {gypsum [$Ca(SO_4)\cdot 2H_2O$], bassanite [$Ca(SO_4)\cdot 0.5H_2O$], and anhydrite [$Ca(SO_4)$]} are important mark-

ers for evaporative and diagenetic processes and fluid chemistry, aiding in reconstructing past water activity and temperature in an environment [28,55]. Other phases for exploration include halides [e.g., halite (NaCl) and sylvite (KCl)], oxides {e.g., corundum structure [hematite (Fe_2O_3), ilmenite ($Fe^{2+}Ti^{4+}O_3$), geikielite ($MgTiO_3$)] and rutile structure [rutile (TiO_2), pyrolusite (MnO_2)]}, and silicates (e.g., amphibole, garnet)

4.6.3. Expanding to Other Planets

Exploring the crystal chemistry of minerals in situ by means of XRD is not only critical for understanding the formation and evolution of Mars, but arguably of even greater importance for Venus and Mercury. Mars is the only planet in our solar system whose mineral composition can be studied on Earth in the form of martian meteorites. The chemical and mineralogical analysis of these crustal fragments excavated by impacts on Mars that found their way to Earth allowed the estimation of the global interior structure, composition, and mantle dynamics of our neighboring planet in the Pre-InSight era [147–149]. No Venusian meteorite has ever been found on Earth [150], and there is also considerable doubt surrounding the putative Mercurian meteorite NWA 7325 [151]. Thus, the only way to access reliable chemical and mineralogical information on the crust of the innermost planets in our solar system is in situ by means of XRD. Studying their surface properties from orbit is particularly challenging because Venus is concealed by a thick atmosphere and exhibits only a few narrow spectral windows [152] that allow light reflected from its surface to be probed, and Mercury exhibits hardly any diagnostic absorption features in the visible and infrared spectral range [153]. In addition, both planets are characterized by extreme environmental conditions which substantially shorten the lifetime of a potential lander mission. These challenges are currently being addressed with the development of a Guinier-type XRD instrument capable of studying multiple samples simultaneously (137-140). This instrument will not only exhibit a higher angular resolution than CheMin—allowing Bragg scattering contributions to be accurately disentangled from various pyroxene phases as well as resulting in an overall improvement in the accuracy of crystal chemical studies—but also enable much faster data collection. Both capabilities combined make these next-generation XRD instruments ideal candidates for future landed missions to Venus and Mercury and could provide us with a first insight into the crystal chemical properties of the crustal rocks of both inner planets which in turn may shed light on their global internal structure and planetary evolution.

5. Conclusions

The comprehensive analysis of Gale crater's mineral composition using the CheMin X-ray diffraction instrument and crystal chemical methods has provided valuable insights into the geological history and mineralogical diversity of this region on Mars. The detection of a variety of minerals, including plagioclase, olivine, pyroxene, and spinel oxides, underscores the complex geological history of Gale crater. The presence of both primary igneous minerals and secondary alteration phases suggests a dynamic environment influenced by both magmatic activity and subsequent aqueous alteration. Therefore, the accurate predictions of mineral compositions further our understanding of the conditions under which these minerals formed. This methodology has proven effective in estimating the compositions of major mineral phases from XRD data, providing a robust framework for future planetary mineralogical studies. Additionally, by comparing the CheMin-analyzed samples with martian meteorites, we have identified similarities and differences that offer clues to the broader geological processes at play on Mars. This comparative approach has helped to contextualize the Gale crater findings within the larger martian geological framework.

These findings not only advance our understanding of martian mineralogy but also contribute to the broader field of planetary science by demonstrating the efficacy of X-ray diffraction coupled with crystal chemical modeling in unraveling the mineralogical history of extraterrestrial bodies. Future work will focus on refining these methodologies and

expanding the dataset to include additional chemical complexity, lower detection limits, additional mineral phases, and other planetary bodies. Additionally, the development of next-generation XRD instruments will further enhance our ability to characterize planetary surfaces with greater precision and efficiency.

Insights gained from this study highlight the importance of in situ mineralogical analysis in planetary exploration and lay the groundwork for future missions aimed at uncovering the mineralogical and geochemical secrets of Mars and beyond.

Supplementary Materials: The following supporting information can be downloaded at https://www.mdpi.com/article/10.3390/min14080773/s1: Table S1: Abundance of crystalline phases detected in Gale crater samples with CheMin; Table S2: Unit-cell parameters of feldspar, olivine, pyroxene, and spinel group mineral phases detected in Gale crater, Mars and analyzed by the CheMin instrument; Table S3: Unit-cell parameters and estimated Ca compositions of plagioclase observed in Gale crater samples by the CheMin instrument; Table S4: Unit-cell parameters and estimated Na compositions and ordering state of alkali feldspar observed in Gale crater samples by the CheMin instrument; Table S5: Unit-cell parameters and estimated Mg compositions of olivine observed in Gale crater samples by the CheMin instrument; Table S6: Unit-cell parameters and estimated Mg, Ca, and Fe compositions of augite observed in Gale crater samples by the CheMin instrument; Table S7: Unit-cell parameters and estimated Mg, Ca, and Fe compositions of pigeonite observed in Gale crater samples by the CheMin instrument; Table S8: Unit-cell parameters and estimated Mg, Ca, and Fe compositions of orthopyroxene observed in Gale crater samples by the CheMin instrument; Table S9: Unit-cell parameters and estimated chemical compositions, as cation apfu, of cubic spinel oxides observed in Gale crater samples by the CheMin instrument.

Author Contributions: Conceptualization, S.M.M.; methodology, S.M.M., R.T.D., A.P. (Anirudh Prabhu) and A.E.; software, S.M.M., S.J.C., A.P. (Anirudh Prabhu) and A.E.; validation, S.M.M.; formal analysis, S.M.M.; investigation, S.M.M.; resources, S.M.M., S.J.C., V.T., A.S.Y., R.T.D., E.B.R., T.F.B., D.F.B., D.T.V., D.W.M., R.V.M., P.I.C., N.C., M.T.T., A.H.T., P.C.S. and A.P. (Aditi Pandey); data curation, S.M.M., S.J.C., R.T.D., E.B.R., T.F.B., D.F.B., D.T.V., M.T.T. and S.L.S.; writing—original draft preparation, S.M.M.; writing—review and editing, S.M.M., R.M.H., S.J.C., J.M.M., V.T., B.M.T., A.R.V. and A.S.Y.; visualization, S.M.M.; project administration, S.M.M.; funding acquisition, S.M.M., R.T.D., T.F.B. and D.F.B. All authors have read and agreed to the published version of the manuscript.

Funding: This research was supported by NASA NNX11AP82A, MSL Investigations, the Carnegie Institution for Science, the 4D Initiative (4d.carnegiescience.edu), and the NASA Astrobiology Institute (Cycle 8) ENIGMA: Evolution of Nanomachines In Geospheres and Microbial Ancestors (80NSSC18M0093). Any opinions, findings, or recommendations expressed herein are those of the authors and do not necessarily reflect the views of the National Aeronautics and Space Administration.

Data Availability Statement: All data collected by the CheMin instrument are available in the Planetary Data System (PDS) Geoscience Node (https://pds-geosciences.wustl.edu/missions/msl/chemin.htm) and the CheMin Database (https://odr.io/chemin). The crystal chemical algorithms and supporting mineral data can be found at https://github.com/shaunnamm/regression-and-minimization (accessed on 1 June 2023) and in the work of Morrison et al. (2018a) [8].

Acknowledgments: We acknowledge the support of the JPL engineering and Mars Science Laboratory (MSL) operations team. We thank the reviewers of this manuscript for their insightful and constructive feedback.

Conflicts of Interest: The authors declare no conflicts of interest. These data and part of their analysis were performed in the course of the NASA-funded and -led Mars Science Laboratory mission; however, as a funder, NASA had no role in the design of the study, interpretation of data, writing of the manuscript, or decision to publish the results. Philippe C. Sarrazin is employees of eXaminArt, Mountain View. The paper reflects the views of the scientists and not the company.

References

1. Grotzinger, J.P. Analysis of Surface Materials by the Curiosity Mars Rover. *Science* **2013**, *341*, 1475. [CrossRef] [PubMed]
2. Martin, P.E.; Farley, K.A.; Baker, M.B.; Malespin, C.A.; Schwenzer, S.P.; Cohen, B.A.; Mahaffy, P.R.; McAdam, A.C.; Ming, D.W.; Vasconcelos, P.M.; et al. A Two-Step K-Ar Experiment on Mars: Dating the Diagenetic Formation of Jarosite from Amazonian Groundwaters. *J. Geophys. Res. Planets* **2017**, *122*, 2803–2818. [CrossRef]

3. Rampe, E.B.; Blake, D.F.; Bristow, T.F.; Ming, D.W.; Vaniman, D.T.; Morris, R.V.; Achilles, C.N.; Chipera, S.J.; Morrison, S.M.; Tu, V.M.; et al. Mineralogy and Geochemistry of Sedimentary Rocks and Eolian Sediments in Gale Crater, Mars: A Review after Six Earth Years of Exploration with Curiosity. *Geochemistry* **2020**, *80*, 125605. [CrossRef]
4. Thomson, B.J.; Bridges, N.T.; Milliken, R.; Baldridge, A.; Hook, S.J.; Crowley, J.K.; Marion, G.M.; de Souza Filho, C.R.; Brown, A.J.; Weitz, C.M. Constraints on the Origin and Evolution of the Layered Mound in Gale Crater, Mars Using Mars Reconnaissance Orbiter Data. *Icarus* **2011**, *214*, 413–432. [CrossRef]
5. Blake, D.; Vaniman, D.; Achilles, C.; Anderson, R.; Bish, D.; Bristow, T.; Chen, C.; Chipera, S.; Crisp, J.; Des Marais, D.; et al. Characterization and Calibration of the CheMin Mineralogical Instrument on Mars Science Laboratory. *Space Sci. Rev.* **2012**, *170*, 341–399. [CrossRef]
6. Blake, D.F.; Morris, R.V.; Kocurek, G.; Morrison, S.M.; Downs, R.T.; Bish, D.; Ming, D.W.; Edgett, K.S.; Rubin, D.; Goetz, W.; et al. Curiosity at Gale Crater, Mars: Characterization and Analysis of the Rocknest Sand Shadow. *Science* **2013**, *341*, 1239505. [CrossRef] [PubMed]
7. Bish, D.L.; Blake, D.F.; Vaniman, D.T.; Chipera, S.J.; Morris, R.V.; Ming, D.W.; Treiman, A.H.; Sarrazin, P.; Morrison, S.M.; Downs, R.T.; et al. X-ray Diffraction Results from Mars Science Laboratory: Mineralogy of Rocknest at Gale Crater. *Science* **2013**, *341*, 1238932. [CrossRef] [PubMed]
8. Morrison, S.M.; Downs, R.T.; Blake, D.F.; Prabhu, A.; Eleish, A.; Vaniman, D.T.; Ming, D.W.; Rampe, E.B.; Hazen, R.M.; Achilles, C.N.; et al. Relationships between Unit-Cell Parameters and Composition for Rock-Forming Minerals on Earth, Mars, and Other Extraterrestrial Bodies. *Am. Mineral.* **2018**, *103*, 848–856. [CrossRef]
9. Morrison, S.M.; Downs, R.T.; Blake, D.F.; Vaniman, D.T.; Ming, D.W.; Hazen, R.M.; Treiman, A.H.; Achilles, C.N.; Yen, A.S.; Morris, R.V.; et al. Crystal Chemistry of Martian Minerals from Bradbury Landing through Naukluft Plateau, Gale Crater, Mars. *Am. Mineral.* **2018**, *103*, 857–871. [CrossRef]
10. Achilles, C.N.; Downs, R.T.; Ming, D.W.; Rampe, E.B.; Morris, R.V.; Treiman, A.H.; Morrison, S.M.; Blake, D.F.; Vaniman, D.T.; Ewing, R.C.; et al. Mineralogy of an Active Eolian Sediment from the Namib Dune, Gale Crater, Mars. *J. Geophys. Res. Planets* **2017**, *122*, 2344–2361. [CrossRef]
11. Achilles, C.N.; Rampe, E.B.; Downs, R.T.; Bristow, T.F.; Ming, D.W.; Morris, R.V.; Vaniman, D.T.; Blake, D.F.; Yen, A.S.; McAdam, A.C.; et al. Evidence for Multiple Diagenetic Episodes in Ancient Fluvial-Lacustrine Sedimentary Rocks in Gale Crater, Mars. *J. Geophys. Res. Planets* **2020**, *125*, e2019JE006295. [CrossRef] [PubMed]
12. Bristow, T.F.; Rampe, E.B.; Achilles, C.N.; Blake, D.F.; Chipera, S.J.; Craig, P.; Crisp, J.A.; Des Marais, D.J.; Downs, R.T.; Gellert, R.; et al. Clay Mineral Diversity and Abundance in Sedimentary Rocks of Gale Crater, Mars. *Sci. Adv.* **2018**, *4*, eaar3330. [CrossRef] [PubMed]
13. Bristow, T.F.; Grotzinger, J.P.; Rampe, E.B.; Cuadros, J.; Chipera, S.J.; Downs, G.W.; Fedo, C.M.; Frydenvang, J.; McAdam, A.C.; Morris, R.V.; et al. Brine-Driven Destruction of Clay Minerals in Gale Crater, Mars. *Science* **2021**, *373*, 198–204. [CrossRef] [PubMed]
14. Lewis, K.W.; Peters, S.; Gonter, K.; Morrison, S.; Schmerr, N.; Vasavada, A.R.; Gabriel, T. A Surface Gravity Traverse on Mars Indicates Low Bedrock Density at Gale Crater. *Science* **2019**, *363*, 535–537. [CrossRef]
15. Mangold, N.; Dehouck, E.; Fedo, C.; Forni, O.; Achilles, C.; Bristow, T.; Downs, R.T.; Frydenvang, J.; Gasnault, O.; L'Haridon, J.; et al. Chemical Alteration of Fine-Grained Sedimentary Rocks at Gale Crater. *Icarus* **2019**, *321*, 619–631. [CrossRef]
16. Morris, R.V.; Rampe, E.B.; Vaniman, D.T.; Christoffersen, R.; Yen, A.S.; Morrison, S.M.; Ming, D.W.; Achilles, C.N.; Fraeman, A.A.; Le, L.; et al. Hydrothermal Precipitation of Sanidine (Adularia) Having Full Al,Si Structural Disorder and Specular Hematite at Maunakea Volcano (Hawai'i) and at Gale Crater (Mars). *J. Geophys. Res. Planets* **2020**, *125*, e2019JE006324. [CrossRef]
17. Morris, R.V.; Vaniman, D.T.; Blake, D.F.; Gellert, R.; Chipera, S.J.; Rampe, E.B.; Ming, D.W.; Morrison, S.M.; Downs, R.T.; Treiman, A.H.; et al. Silicic Volcanism on Mars Evidenced by Tridymite in High-SiO_2 Sedimentary Rock at Gale Crater. *Proc. Natl. Acad. Sci. USA* **2016**, *113*, 7071–7076. [CrossRef] [PubMed]
18. Payré, V.; Siebach, K.L.; Dasgupta, R.; Udry, A.; Rampe, E.B.; Morrison, S.M. Constraining Ancient Magmatic Evolution on Mars Using Crystal Chemistry of Detrital Igneous Minerals in the Sedimentary Bradbury Group, Gale Crater, Mars. *J. Geophys. Res. Planets* **2020**, *125*, e2020JE006467. [CrossRef]
19. Rampe, E.B.; Ming, D.W.; Blake, D.F.; Bristow, T.F.; Chipera, S.J.; Grotzinger, J.P.; Morris, R.V.; Morrison, S.M.; Vaniman, D.T.; Yen, A.S.; et al. Mineralogy of an Ancient Lacustrine Mudstone Succession from the Murray Formation, Gale Crater, Mars. *Earth Planet. Sci. Lett.* **2017**, *471*, 172–185. [CrossRef]
20. Rampe, E.B.; Lapotre, M.G.A.; Bristow, T.F.; Arvidson, R.E.; Morris, R.V.; Achilles, C.N.; Weitz, C.; Blake, D.F.; Ming, D.W.; Morrison, S.M.; et al. Sand Mineralogy Within the Bagnold Dunes, Gale Crater, as Observed In Situ and From Orbit. *Geophys. Res. Lett.* **2018**, *45*, 9488–9497. [CrossRef]
21. Treiman, A.H.; Bish, D.L.; Vaniman, D.T.; Chipera, S.J.; Blake, D.F.; Ming, D.W.D.; Morris, R.V.; Bristow, T.F.; Morrison, S.M.; Baker, M.B.; et al. Mineralogy, Provenance, and Diagenesis of a Potassic Basaltic Sandstone on Mars: CheMin X-ray Diffraction of the Windjana Sample (Kimberley Area, Gale Crater). *J. Geophys. Res. Planets* **2016**, *121*, 75–106. [CrossRef] [PubMed]
22. Treiman, A.H.; Morris, R.V.; Agresti, D.G.; Graff, T.G.; Achilles, C.N.; Rampe, E.B.; Bristow, T.F.; Blake, D.F.; Vaniman, D.T.; Bish, D.L.; et al. Ferrian Saponite from the Santa Monica Mountains (California, U.S.A., Earth): Characterization as an Analog for Clay Minerals on Mars with Application to Yellowknife Bay in Gale Crater. *Am. Mineral.* **2014**, *99*, 2234–2250. [CrossRef]
23. Tu, V.M.; Rampe, E.B.; Bristow, T.F.; Thorpe, M.T.; Clark, J.V.; Castle, N.; Fraeman, A.A.; Edgar, L.A.; McAdam, A.; Bedford, C.; et al. A Review of the Phyllosilicates in Gale Crater as Detected by the CheMin Instrument on the Mars Science Laboratory, Curiosity Rover. *Minerals* **2021**, *11*, 847. [CrossRef]

24. Vaniman, D.T.; Bish, D.L.; Ming, D.W.; Bristow, T.F.; Morris, R.V.; Blake, D.F.; Chipera, S.J.; Morrison, S.M.; Treiman, A.H.; Rampe, E.B.; et al. Mineralogy of a Mudstone at Yellowknife Bay, Gale Crater, Mars. *Science* **2014**, *343*, 1243480. [CrossRef]
25. Yen, A.S.; Ming, D.W.; Vaniman, D.T.; Gellert, R.; Blake, D.F.; Morris, R.V.; Morrison, S.M.; Bristow, T.F.; Chipera, S.J.; Edgett, K.S.; et al. Multiple Stages of Aqueous Alteration along Fractures in Mudstone and Sandstone Strata in Gale Crater, Mars. *Earth Planet. Sci. Lett.* **2017**, *471*, 186–198. [CrossRef]
26. Yen, A.S.; Morris, R.V.; Ming, D.W.; Schwenzer, S.P.; Sutter, B.; Vaniman, D.T.; Treiman, A.H.; Gellert, R.; Achilles, C.N.; Berger, J.A.; et al. Formation of Tridymite and Evidence for a Hydrothermal History at Gale Crater, Mars. *J. Geophys. Res. Planets* **2021**, *126*, e2020JE006569. [CrossRef]
27. Thorpe, M.T.; Bristow, T.F.; Rampe, E.B.; Tosca, N.J.; Grotzinger, J.P.; Bennett, K.A.; Achilles, C.N.; Blake, D.F.; Chipera, S.J.; Downs, G.; et al. Mars Science Laboratory CheMin Data From the Glen Torridon Region and the Significance of Lake-Groundwater Interactions in Interpreting Mineralogy and Sedimentary History. *J. Geophys. Res. Planets* **2022**, *127*, e2021JE007099. [CrossRef]
28. Chipera, S.; Vaniman, D.; Rampe, E.; Bristow, T.; Martínez, G.; Tu, V.; Peretyazhko, T.; Yen, A.; Gellert, R.; Berger, J.; et al. Mineralogical Investigation of Mg-Sulfate at the Canaima Drill Site, Gale Crater, Mars. *J. Geophys. Res. Planets* **2023**, *128*, e2023JE008041. [CrossRef]
29. Rampe, E.B.; Bristow, T.F.; Morris, R.V.; Morrison, S.M.; Achilles, C.N.; Ming, D.W.; Vaniman, D.T.; Blake, D.F.; Tu, V.M.; Chipera, S.J.; et al. Mineralogy of Vera Rubin Ridge From the Mars Science Laboratory CheMin Instrument. *J. Geophys. Res. Planets* **2020**, *125*, e2019JE006306. [CrossRef]
30. Vaniman, D.T.; Martínez, G.M.; Rampe, E.B.; Bristow, T.F.; Blake, D.F.; Yen, A.S.; Ming, D.W.; Rapin, W.; Meslin, P.-Y.; Morookian, J.M.; et al. Gypsum, Bassanite, and Anhydrite at Gale Crater, Mars. *Am. Mineral.* **2018**, *103*, 1011–1020. [CrossRef]
31. McLennan, S.M.; Grotzinger, J.P.; Hurowitz, J.A.; Tosca, N.J. The Sedimentary Cycle on Early Mars. *Annu. Rev. Earth Planet. Sci.* **2019**, *47*, 91–118. [CrossRef]
32. McAdam, A.C.; Sutter, B.; Archer, P.D.; Franz, H.B.; Wong, G.M.; Lewis, J.M.T.; Eigenbrode, J.L.; Stern, J.C.; Knudson, C.A.; Clark, J.V.; et al. Constraints on the Mineralogy and Geochemistry of Vera Rubin Ridge, Gale Crater, Mars, From Mars Science Laboratory Sample Analysis at Mars Evolved Gas Analyses. *J. Geophys. Res. Planets* **2020**, *125*, e2019JE006309. [CrossRef]
33. Tarnas, J.; Mustard, J.; Lollar, B.S.; Stamenković, V.; Cannon, K.; Lorand, J.-P.; Onstott, T.; Michalski, J.; Warr, O.; Palumbo, A.; et al. Earth-like Habitable Environments in the Subsurface of Mars. *Astrobiology* **2021**, *21*, 741–756. [CrossRef] [PubMed]
34. Bedford, C.C.; Schwenzer, S.P.; Bridges, J.C.; Banham, S.; Wiens, R.C.; Gasnault, O.; Rampe, E.B.; Frydenvang, J.; Gasda, P.J. Geochemical Variation in the Stimson Formation of Gale Crater: Provenance, Mineral Sorting, and a Comparison with Modern Martian Dunes. *Icarus* **2020**, *341*, 113622. [CrossRef]
35. Bedford, C.C.; Banham, S.G.; Bridges, J.C.; Forni, O.; Cousin, A.; Bowden, D.; Turner, S.M.R.; Wiens, R.C.; Gasda, P.J.; Frydenvang, J.; et al. An Insight into Ancient Aeolian Processes and Post-Noachian Aqueous Alteration in Gale Crater, Mars, Using ChemCam Geochemical Data from the Greenheugh Capping Unit. *J. Geophys. Res. Planets* **2022**, *127*, e2021JE007100. [CrossRef]
36. Bedford, C.C.; Bridges, J.C.; Schwenzer, S.P.; Wiens, R.C.; Rampe, E.B.; Frydenvang, J.; Gasda, P.J. Alteration Trends and Geochemical Source Region Characteristics Preserved in the Fluviolacustrine Sedimentary Record of Gale Crater, Mars. *Geochim. Cosmochim. Acta* **2019**, *246*, 234–266. [CrossRef]
37. Fraeman, A.A.; Johnson, J.R.; Arvidson, R.E.; Rice, M.S.; Wellington, D.F.; Morris, R.V.; Fox, V.K.; Horgan, B.H.N.; Jacob, S.R.; Salvatore, M.R.; et al. Synergistic Ground and Orbital Observations of Iron Oxides on Mt. Sharp and Vera Rubin Ridge. *J. Geophys. Res. Planets* **2020**, *125*, e2019JE006294. [CrossRef] [PubMed]
38. David, G.; Cousin, A.; Forni, O.; Meslin, P.-Y.; Dehouck, E.; Mangold, N.; L'Haridon, J.; Rapin, W.; Gasnault, O.; Johnson, J.R.; et al. Analyses of High-Iron Sedimentary Bedrock and Diagenetic Features Observed with ChemCam at Vera Rubin Ridge, Gale Crater, Mars: Calibration and Characterization. *J. Geophys. Res. Planets* **2020**, *125*, e2019JE006314. [CrossRef]
39. Smith, R.J.; McLennan, S.M.; Achilles, C.N.; Dehouck, E.; Horgan, B.H.N.; Mangold, N.; Rampe, E.B.; Salvatore, M.; Siebach, K.L.; Sun, V. X-ray Amorphous Components in Sedimentary Rocks of Gale Crater, Mars: Evidence for Ancient Formation and Long-Lived Aqueous Activity. *J. Geophys. Res. Planets* **2021**, *126*, e2020JE006782. [CrossRef]
40. Fukushi, K.; Sekine, Y.; Sakuma, H.; Morida, K.; Wordsworth, R. Semiarid Climate and Hyposaline Lake on Early Mars Inferred from Reconstructed Water Chemistry at Gale. *Nat. Commun.* **2019**, *10*, 4896. [CrossRef]
41. Fornaro, T.; Boosman, A.; Brucato, J.R.; ten Kate, I.L.; Siljeström, S.; Poggiali, G.; Steele, A.; Hazen, R.M. UV Irradiation of Biomarkers Adsorbed on Minerals under Martian-like Conditions: Hints for Life Detection on Mars. *Icarus* **2018**, *313*, 38–60. [CrossRef]
42. David, G.; Meslin, P.-Y.; Dehouck, E.; Gasnault, O.; Cousin, A.; Forni, O.; Berger, G.; Lasue, J.; Pinet, P.; Wiens, R.C.; et al. Laser-Induced Breakdown Spectroscopy (LIBS) Characterization of Granular Soils: Implications for ChemCam Analyses at Gale Crater, Mars. *Icarus* **2021**, *365*, 114481. [CrossRef]
43. Hogancamp, J.V.; Sutter, B.; Morris, R.V.; Archer, P.D.; Ming, D.W.; Rampe, E.B.; Mahaffy, P.; Navarro-Gonzalez, R. Chlorate/Fe-Bearing Phase Mixtures as a Possible Source of Oxygen and Chlorine Detected by the Sample Analysis at Mars Instrument in Gale Crater, Mars. *J. Geophys. Res. Planets* **2018**, *123*, 2920–2938. [CrossRef]
44. Zhong, J.Q.; Fiore, S.; Chen, X.X.; Zhou, C.H. Enigmatic Issues and Widening Implications of Research on Martian Clay Minerals. *ACS Earth Space Chem.* **2022**, *6*, 2118–2141. [CrossRef]
45. Rizzo, V.; Armstrong, R.; Hua, H.; Cantasano, N.; Nicolò, T.; Bianciardi, G. Life on Mars: Clues, Evidence or Proof? In *Solar System Planets and Exoplanets*; IntechOpen: London, UK, 2021; ISBN 1-83969-313-4.

46. Ralston, S.; Hausrath, E.M.; Tschauner, O.; Rampe, E.; Peretyazhko, T.S.; Christoffersen, R.; Defelice, C.; Lee, H. Dissolution Rates of Allophane with Variable Fe Contents: Implications for Aqueous Alteration and the Preservation of X-ray Amorphous Materials on Mars. *Clays Clay Miner.* **2021**, *69*, 263–288. [CrossRef]
47. Sheppard, R.Y.; Thorpe, M.T.; Fraeman, A.A.; Fox, V.K.; Milliken, R.E. Merging Perspectives on Secondary Minerals on Mars: A Review of Ancient Water-Rock Interactions in Gale Crater Inferred from Orbital and in-Situ Observations. *Minerals* **2021**, *11*, 986. [CrossRef]
48. Wong, G.M.; Franz, H.B.; Clark, J.V.; McAdam, A.C.; Lewis, J.M.; Millan, M.; Ming, D.W.; Gomez, F.; Clark, B.; Eigenbrode, J.L.; et al. Oxidized and Reduced Sulfur Observed by the Sample Analysis at Mars (SAM) Instrument Suite on the Curiosity Rover within the Glen Torridon Region at Gale Crater, Mars. *J. Geophys. Res. Planets* **2022**, *127*, e2021JE007084. [CrossRef]
49. Smith, R.; McLennan, S.; Sutter, B.; Rampe, E.; Dehouck, E.; Siebach, K.; Horgan, B.; Sun, V.; McAdam, A.; Mangold, N.; et al. X-ray Amorphous Sulfur-Bearing Phases in Sedimentary Rocks of Gale Crater, Mars. *J. Geophys. Res. Planets* **2022**, *127*, e2021JE007128. [CrossRef]
50. Turner, S.M.; Schwenzer, S.; Bridges, J.; Rampe, E.; Bedford, C.; Achilles, C.; McAdam, A.; Mangold, N.; Hicks, L.; Parnell, J.; et al. Early Diagenesis at and below Vera Rubin Ridge, Gale Crater, Mars. *Meteorit. Planet. Sci.* **2021**, *56*, 1905–1932. [CrossRef]
51. Kite, E.S.; Daswani, M.M. Geochemistry Constrains Global Hydrology on Early Mars. *Earth Planet. Sci. Lett.* **2019**, *524*, 115718. [CrossRef]
52. Pandey, A.; Rampe, E.B.; Ming, D.W.; Deng, Y.; Bedford, C.C.; Schwab, P. Quantification of Amorphous Si, Al, and Fe in Palagonitic Mars Analogs by Chemical Extraction and X-ray Spectroscopy. *Icarus* **2023**, *392*, 115362. [CrossRef]
53. Payré, V.; Fabre, C.; Sautter, V.; Cousin, A.; Mangold, N.; Le Deit, L.; Forni, O.; Goetz, W.; Wiens, R.C.; Gasnault, O.; et al. Copper Enrichments in the Kimberley Formation in Gale Crater, Mars: Evidence for a Cu Deposit at the Source. *Icarus* **2019**, *321*, 736–751. [CrossRef]
54. Hazen, R.M.; Morrison, S.M. On the Paragenetic Modes of Minerals: A Mineral Evolution Perspective. *Am. Mineral.* **2022**, *107*, 1262–1287. [CrossRef]
55. Hazen, R.M.; Downs, R.T.; Morrison, S.M.; Tutolo, B.M.; Blake, D.F.; Bristow, T.F.; Chipera, S.J.; McSween, H.Y.; Ming, D.; Morris, R.V.; et al. On the Diversity and Formation Modes of Martian Minerals. *J. Geophys. Res. Planets* **2023**, *128*, e2023JE007865. [CrossRef]
56. Hazen, R.M.; Morrison, S.M. An Evolutionary System of Mineralogy, Part I: Stellar Mineralogy (>13 to 4.6 Ga). *Am. Mineral.* **2020**, *105*, 627–651. [CrossRef]
57. Morrison, S.M.; Hazen, R.M. An Evolutionary System of Mineralogy. Part II: Interstellar and Solar Nebula Primary Condensation Mineralogy (>4.565 Ga). *Am. Mineral.* **2020**, *105*, 1508–1535. [CrossRef]
58. Hazen, R.M.; Morrison, S.M.; Prabhu, A. An Evolutionary System of Mineralogy, Part III: Primary Chondrule Mineralogy (4566 to 4561 Ma). *Am. Mineral.* **2020**, *106*, 325–350. [CrossRef]
59. Morrison, S.M.; Hazen, R.M. An Evolutionary System of Mineralogy, Part IV: Planetesimal Differentiation and Impact Mineralization (4566 to 4560 Ma). *Am. Mineral.* **2020**, *106*, 730–761. [CrossRef]
60. Hazen, R.M.; Morrison, S.M. An Evolutionary System of Mineralogy, Part V: Aqueous and Thermal Alteration of Planetesimals (~4565 to 4550 Ma). *Am. Mineral.* **2020**, *106*, 1388–1419. [CrossRef]
61. Morrison, S.M.; Prabhu, A.; Hazen, R.M. An Evolutionary System of Mineralogy, Part VI: Earth's Earliest Hadean Crust (>4370 Ma). *Am. Mineral.* **2022**, *108*, 42–58. [CrossRef]
62. Hazen, R.M.; Morrison, S.M.; Prabhu, A.; Walter, M.; Williams, J. An Evolutionary System of Mineralogy, Part VII: The Evolution of the Igneous Minerals (>2500 Ma). *Am. Mineral.* **2023**, *108*, 1620–1641. [CrossRef]
63. Hazen, R.M.; Morrison, S.M.; Krivovichev, S.V.; Downs, R.T. Lumping and Splitting: Toward a Classification of Mineral Natural Kinds. *Am. Mineral.* **2022**, *107*, 1288–1301. [CrossRef]
64. Tutolo, B.M.; Hausrath, E.; Thorpe, M.; Rampe, E.B.; Bristow, T.; Blake, D.F.; Vaniman, D.T.; Morrison, S.M.; Chipera, S.; Downs, R.T.; et al. In Situ Evidence of an Active Carbon Cycle on Ancient Mars. In Proceedings of the GSA Connects 2023 Meeting, Pittsburgh, PA, USA, 15–18 October 2023.
65. Tutolo, B.M.; Hausrath, E.M.; Rampe, E.B.; Bristow, T.F.; Downs, R.T.; Kite, E.; Peretyazhko, T.; Thorpe, M.T.; Grotzinger, J.; Archer, D.; et al. In Situ Evidence for an Active Carbon Cycle on Ancient Mars. In Proceedings of the 55th Lunar and Planetary Science Conference, The Woodlands, TX, USA, 11–15 March 2024; 3040. p. 1564.
66. Blake, D.; Tu, V.; Bristow, T.; Rampe, E.; Vaniman, D.; Chipera, S.; Sarrazin, P.; Morris, R.; Morrison, S.; Yen, A.; et al. The Chemistry and Mineralogy (CheMin) X-ray Diffractometer on the MSL Curiosity Rover: A Decade of Mineralogy from Gale Crater, Mars. *Minerals* **2024**, *14*, 568. [CrossRef]
67. Young, R. (Ed.) *The Rietveld Method*; International Union of Crystallography; Oxford University Press: Oxford, UK, 1993.
68. Rietveld, H.M. A Profile Refinement Method for Nuclear and Magnetic Structures. *J. Appl. Crystallogr.* **1969**, *2*, 65–71. [CrossRef]
69. Bish, D.L.; Howard, S. Quantitative Phase Analysis Using the Rietveld Method. *J. Appl. Crystallogr.* **1988**, *21*, 86–91.
70. Jenkins, R. Modern Powder Diffraction. *Rev. Miner.* **1989**, *20*, 47–72.
71. Chipera, S.J.; Bish, D.L. Fitting Full X-ray Diffraction Patterns for Quantitative Analysis: A Method for Readily Quantifying Crystalline and Disordered Phases. *Adv. Mater. Phys. Chem.* **2013**, *3*, 47–53. [CrossRef]
72. Chipera, S.J.; Bish, D.L. FULLPAT: A Full-Pattern Quantitative Analysis Program for X-ray Powder Diffraction Using Measured and Calculated Patterns. *J. Appl. Crystallogr.* **2002**, *35*, 744–749. [CrossRef]

73. Papike, J.J.; Karner, J.M.; Shearer, C.K.; Burger, P.V. Silicate Mineralogy of Martian Meteorites. *Geochim. Cosmochim. Acta* **2009**, *73*, 7443–7485. [CrossRef]
74. Santos, A.R.; Agee, C.B.; McCubbin, F.M.; Shearer, C.K.; Burger, P.V.; Tartèse, R.; Anand, M. Petrology of Igneous Clasts in Northwest Africa 7034: Implications for the Petrologic Diversity of the Martian Crust. *Geochim. Cosmochim. Acta* **2015**, *157*, 56–85. [CrossRef]
75. Wittmann, A.; Korotev, R.L.; Jolliff, B.L.; Irving, A.J.; Moser, D.E.; Barker, I.; Rumble, D., III. Petrography and Composition of Martian Regolith Breccia Meteorite Northwest Africa 7475. *Meteorit. Planet. Sci.* **2015**, *50*, 326–352. [CrossRef]
76. Nyquist, L.E.; Shih, C.Y.; Mccubbin, F.M.; Santos, A.R.; Shearer, C.K.; Peng, Z.X.; Burger, P.V.; Agee, C.B. Rb-Sr and Sm-Nd Isotopic and REE Studies of Igneous Components in the Bulk Matrix Domain of Martian Breccia Northwest Africa 7034. *Meteorit. Planet. Sci.* **2016**, *51*, 483–498. [CrossRef]
77. Hewins, R.H.; Zanda, B.; Humayun, M.; Nemchin, A.; Lorand, J.P.; Pont, S.; Deldicque, D.; Bellucci, J.J.; Beck, P.; Leroux, H.; et al. Regolith Breccia Northwest Africa 7533: Mineralogy and Petrology with Implications for Early Mars. *Meteorit. Planet. Sci.* **2017**, *52*, 89–124. [CrossRef]
78. Kroll, H. Lattice Parameters and Determinative Methods for Plagioclase and Ternary Feldspars. In *Mineralogical Society of America Reviews in Mineralogy*; De Gruyter: Berlin, Germany, 1983; pp. 101–119.
79. Smith, J.V.; Brown, W.L. *Crystal Structures, Physical, Chemical, and Microtextural Properties*, 2nd ed.; Springer: Berlin/Heidelberg, Germany, 1988.
80. Lehnert, K.A.; Ji, P.; Mays, J.; Figueroa, J.D.; Johansson, A.; Profeta, L.; Song, L.; Richard, S.; Morrison, S.; Ostroverkhova, A. The Astromaterials Data System: Advancing Access and Preservation of Past, Present, and Future Lab Analytical Data of NASA'S Astromaterials Collections. In Proceedings of the Astromaterials Data Management in the Era of Sample-Return Missions Community Workshop, Arizona, AZ, USA, 8–9 November 2021; p. id.2025.
81. Mustard, J.; Poulet, F.; Gendrin, A.; Bibring, J.-P.; Langevin, Y.; Gondet, B.; Mangold, N.; Bellucci, G.; Altieri, F. Olivine and Pyroxene Diversity in the Crust of Mars. *Science* **2005**, *307*, 1594–1597. [CrossRef]
82. McSween, H.Y., Jr.; Head, J.W., III; Rogers, A.D.; Schmidt, M.E. Assessing Global Trends in Mars Magma Compositions Using Ground Truth. *Meteorit. Planet. Sci.* **2023**, *58*, 1306–1317. [CrossRef]
83. Turnock, A.C.; Lindsley, D.H.; Grover, J.E. Synthesis and Unit Cell Parameters of Ca-Mg-Fe Pyroxenes. *Am. Mineral.* **1973**, *58*, 50–59.
84. Lindsley, D.H. Pyroxene Thermometry. *Am. Mineral.* **1983**, *68*, 477–493. [CrossRef]
85. Treiman, A.H.; Irving, A.J. Petrology of Martian Meteorite Northwest Africa 998. *Meteorit. Planet. Sci.* **2008**, *43*, 829–854. [CrossRef]
86. Morrison, S.M.; Cantoni, A.; Prabhu, A.; Udry, A.; Hazen, R.; Ostroverkhova, A. Exploring Martian Geology and Habitability via Mineral Network Analysis. In Proceedings of the AGU Fall Meeting 2022, Chicago, IL, USA, 12–16 December 2022.
87. Liu, Y.; Floss, C.; Day, J.M.; Hill, E.; Taylor, L.A. Petrogenesis of Lunar Mare Basalt Meteorite Miller Range 05035. *Meteorit. Planet. Sci.* **2009**, *44*, 261–284. [CrossRef]
88. Borromeo, L.; Andò, S.; Bersani, D.; Garzanti, E.; Gentile, P.; Mantovani, L.; Tribaudino, M. How to Identify Pigeonite: A Raman and SEM-EDS Study of Detrital Ca-Poor Clinopyroxene from Continental Flood Basalts. *Chem. Geol.* **2023**, *635*, 121610. [CrossRef]
89. Tosca, N.J.; Ahmed, I.A.; Tutolo, B.M.; Ashpitel, A.; Hurowitz, J.A. Magnetite Authigenesis and the Warming of Early Mars. *Nat. Geosci.* **2018**, *11*, 635–639. [PubMed]
90. Goodrich, C.A.; Herd, C.D.; Taylor, L.A. Spinels and Oxygen Fugacity in Olivine-phyric and Lherzolitic Shergottites. *Meteorit. Planet. Sci.* **2003**, *38*, 1773–1792. [CrossRef]
91. Ikeda, Y. Petrology of Magmatic Silicate Inclusions in the Allan Hills 77005 Lherzolitic Shergottite. *Meteorit. Planet. Sci.* **1998**, *33*, 803–812.
92. Mittlefehldt, D.W. ALH84001, a Cumulate Orthopyroxenite Member of the Martian Meteorite Clan. *Meteoritics* **1994**, *29*, 214–221.
93. Shearer, C.; Leshin, L.; Adcock, C. Olivine in Martian Meteorite Allan Hills 84001: Evidence for a High-temperature Origin and Implications for Signs of Life. *Meteorit. Planet. Sci.* **1999**, *34*, 331–339.
94. Floran, R.; Prinz, M.; Hlava, P.; Keil, K.; Nehru, C.; Hinthorne, J. The Chassigny Meteorite: A Cumulate Dunite with Hydrous Amphibole-Bearing Melt Inclusions. *Geochim. Cosmochim. Acta* **1978**, *42*, 1213–1229. [CrossRef]
95. Johnson, M.C.; Rutherford, M.J.; Hess, P.C. Chassigny Petrogenesis: Melt Compositions, Intensive Parameters and Water Contents of Martian (?) Magmas. *Geochim. Cosmochim. Acta* **1991**, *55*, 349–366. [CrossRef]
96. Folco, L.; Franchi, I.; D'Orazio, M.; Rocchi, S.; Schultz, L. A New Martian Meteorite from the Sahara: The Shergottite Dar al Gani 489. *Meteorit. Planet. Sci.* **2000**, *35*, 827–839.
97. Wadhwa, M.; Lentz, R.; McSween, H., Jr.; Crozaz, G. A Petrologic and Trace Element Study of Dar al Gani 476 and Dar al Gani 489: Twin Meteorites with Affinities to Basaltic and Lherzolitic Shergottites. *Meteorit. Planet. Sci.* **2001**, *36*, 195–208. [CrossRef]
98. Zipfel, J.; Scherer, P.; Spettel, B.; Dreibus, G.; Schultz, L. Petrology and Chemistry of the New Shergottite Dar al Gani 476. *Meteorit. Planet. Sci.* **2000**, *35*, 95–106. [CrossRef]
99. Mikouchi, T.; Miyamoto, M. Mineralogy and Olivine Cooling Rate of the Dhofar 019 Shergottite. *Antarct. Meteor. Res.* **2002**, *15*, 122.
100. Taylor, L.; Nazarov, M.; Shearer, C.; McSween Jr, H.; Cahill, J.; Neal, C.; Ivanova, M.; Barsukova, L.; Lentz, R.; Clayton, R.; et al. Martian Meteorite Dhofar 019: A New Shergottite. *Meteorit. Planet. Sci.* **2002**, *37*, 1107–1128. [CrossRef]

101. Ikeda, Y.; Kimura, M.; Takeda, H.; Shimoda, G.; Kita, N.T.; Morishita, Y.; Suzuki, A.; Jagoutz, E.; Dreibus, G. Petrology of a New Basaltic Shergottite: Dhofar 378. *Antarct. Meteor. Res.* **2006**, *19*, 20–44.
102. Goodrich, C.A. Petrogenesis of Olivine-Phyric Shergottites Sayh al Uhaymir 005 and Elephant Moraine A79001 Lithology A. *Geochim. Cosmochim. Acta* **2003**, *67*, 3735–3772. [CrossRef]
103. McSween, H.Y., Jr.; Jarosewich, E. Petrogenesis of the Elephant Moraine A79001 Meteorite: Multiple Magma Pulses on the Shergottite Parent Body. *Geochim. Cosmochim. Acta* **1983**, *47*, 1501–1513. [CrossRef]
104. Steele, I.M.; Smith, J.V. Petrography and Mineralogy of Two Basalts and Olivine-pyroxene-spinel Fragments in Achondrite EETA79001. *J. Geophys. Res. Solid Earth* **1982**, *87*, A375–A384. [CrossRef]
105. Jiang, Y.; Hsu, W. Petrogenesis of Grove Mountains 020090: An Enriched "Lherzolitic" Shergottite. *Meteorit. Planet. Sci.* **2012**, *47*, 1419–1435. [CrossRef]
106. Lin, Y.; Hu, S.; Miao, B.; Xu, L.; Liu, Y.; Xie, L.; Feng, L.; Yang, J. Grove Mountains 020090 Enriched Lherzolitic Shergottite: A Two-stage Formation Model. *Meteorit. Planet. Sci.* **2013**, *48*, 1572–1589. [CrossRef]
107. Lin, Y.; Guan, Y.; Wang, D.; Kimura, M.; Leshin, L.A. Petrogenesis of the New Lherzolitic Shergottite Grove Mountains 99027: Constraints of Petrography, Mineral Chemistry, and Rare Earth Elements. *Meteorit. Planet. Sci.* **2005**, *40*, 1599–1619. [CrossRef]
108. Bunch, T.; Reid, A.M. The Nakhlites Part I: Petrography and Mineral Chemistry. *Meteoritics* **1975**, *10*, 303–315. [CrossRef]
109. Szymanski, A.; Brenker, F.E.; Palme, H.; El Goresy, A. High Oxidation State during Formation of Martian Nakhlites. *Meteorit. Planet. Sci.* **2010**, *45*, 21–31. [CrossRef]
110. Balta, J.B.; Sanborn, M.; McSween, H.Y., Jr.; Wadhwa, M. Magmatic History and Parental Melt Composition of Olivine-phyric Shergottite LAR 06319: Importance of Magmatic Degassing and Olivine Antecrysts in Martian Magmatism. *Meteorit. Planet. Sci.* **2013**, *48*, 1359–1382. [CrossRef]
111. Peslier, A.; Hnatyshin, D.; Herd, C.D.; Walton, E.L.; Brandon, A.D.; Lapen, T.; Shafer, J. Crystallization, Melt Inclusion, and Redox History of a Martian Meteorite: Olivine-Phyric Shergottite Larkman Nunatak 06319. *Geochim. Cosmochim. Acta* **2010**, *74*, 4543–4576. [CrossRef]
112. Sarbadhikari, A.B.; Day, J.M.; Liu, Y.; Rumble, D., III; Taylor, L.A. Petrogenesis of Olivine-Phyric Shergottite Larkman Nunatak 06319: Implications for Enriched Components in Martian Basalts. *Geochim. Cosmochim. Acta* **2009**, *73*, 2190–2214. [CrossRef]
113. Gleason, J.D.; Kring, D.A.; Hill, D.H.; Boynton, W.V. Petrography and Bulk Chemistry of Martian Lherzolite LEW88516. *Geochim. Cosmochim. Acta* **1997**, *61*, 4007–4014. [CrossRef]
114. Harvey, R.; Wadhwa, M.; McSween, H.Y., Jr.; Crozaz, G. Petrography, Mineral Chemistry, and Petrogenesis of Antarctic Shergottite LEW88516. *Geochim. Cosmochim. Acta* **1993**, *57*, 4769–4783.
115. Treiman, A.; McKay, G.; Bogard, D.; Mittlefehldt, D.; Wang, M.; Keller, L.; Lipschutz, M.; Lindstrom, M.; Garrison, D. Comparison of the LEW88516 and ALHA77005 Martian Meteorites: Similar but Distinct. *Meteoritics* **1994**, *29*, 581–592. [CrossRef]
116. Mikouchi, T. Mineralogical Similarities and Differences between the Los Angeles Basaltic Shergottite and the Asuka-881757 Lunar Mare Meteorite. *Antarct. Meteor. Res.* **2001**, *14*, 1.
117. Warren, P.H.; Greenwood, J.P.; Rubin, A.E. Los Angeles: A Tale of Two Stones. *Meteorit. Planet. Sci.* **2004**, *39*, 137–156. [CrossRef]
118. Day, J.M.; Taylor, L.A.; Floss, C.; McSween, H.Y., Jr. Petrology and Chemistry of MIL 03346 and Its Significance in Understanding the Petrogenesis of Nakhlites on Mars. *Meteorit. Planet. Sci.* **2006**, *41*, 581–606. [CrossRef]
119. Imae, N.; Ikeda, Y. Petrology of the Miller Range 03346 Nakhlite in Comparison with the Yamato-000593 Nakhlite. *Meteorit. Planet. Sci.* **2007**, *42*, 171–184. [CrossRef]
120. Udry, A.; McSween, H.Y., Jr.; Lecumberri-Sanchez, P.; Bodnar, R.J. Paired Nakhlites MIL 090030, 090032, 090136, and 03346: Insights into the Miller Range Parent Meteorite. *Meteorit. Planet. Sci.* **2012**, *47*, 1575–1589. [CrossRef]
121. Sautter, V.; Barrat, J.; Jambon, A.; Lorand, J.; Gillet, P.; Javoy, M.; Joron, J.; Lesourd, M. A New Martian Meteorite from Morocco: The Nakhlite North West Africa 817. *Earth Planet. Sci. Lett.* **2002**, *195*, 223–238.
122. Jambon, A.; Barrat, J.; Sautter, V.; Gillet, P.; Göpel, C.; Javoy, M.; Joron, J.; Lesourd, M. The Basaltic Shergottite Northwest Africa 856: Petrology and Chemistry. *Meteorit. Planet. Sci.* **2002**, *37*, 1147–1164.
123. Barrat, J.; Jambon, A.; Bohn, M.; Gillet, P.; Sautter, V.; Göpel, C.; Lesourd, M.; Keller, F. Petrology and Chemistry of the Picritic Shergottite North West Africa 1068 (NWA 1068). *Geochim. Cosmochim. Acta* **2002**, *66*, 3505–3518. [CrossRef]
124. Gillet, P.; Barrat, J.-A.; Beck, P.; Marty, B.; Greenwood, R.; Franchi, I.; Bohn, M.; Cotten, J. Petrology, Geochemistry, and Cosmic-ray Exposure Age of Iherzolitic Shergottite Northwest Africa 1950. *Meteorit. Planet. Sci.* **2005**, *40*, 1175–1184.
125. Mikouchi, T. Northwest Africa 1950: Mineralogy and Comparison with Antarctic Lherzolitic Shergottites. *Meteorit. Planet. Sci.* **2005**, *40*, 1621–1634.
126. Beck, P.; Barrat, J.-A.; Gillet, P.; Wadhwa, M.; Franchi, I.; Greenwood, R.; Bohn, M.; Cotten, J.; van de Moortèle, B.; Reynard, B. Petrography and Geochemistry of the Chassignite Northwest Africa 2737 (NWA 2737). *Geochim. Cosmochim. Acta* **2006**, *70*, 2127–2139.
127. Treiman, A.H.; Dyar, M.D.; McCanta, M.; Noble, S.K.; Pieters, C.M. Martian Dunite NWA 2737: Petrographic Constraints on Geological History, Shock Events, and Olivine Color. *J. Geophys. Res. Planets* **2007**, *112*, e2006JE002777.
128. Gross, J.; Treiman, A.H.; Filiberto, J.; Herd, C.D. Primitive Olivine-phyric Shergottite NWA 5789: Petrography, Mineral Chemistry, and Cooling History Imply a Magma Similar to Yamato-980459. *Meteorit. Planet. Sci.* **2011**, *46*, 116–133. [CrossRef]
129. Brian Balta, J.; Sanborn, M.E.; Mayne, R.G.; Wadhwa, M.; McSween, H.Y., Jr.; Crossley, S.D. Northwest Africa 5790: A Previously Unsampled Portion of the Upper Part of the Nakhlite Pile. *Meteorit. Planet. Sci.* **2017**, *52*, 36–59. [CrossRef]

130. Howarth, G.H.; Pernet-Fisher, J.F.; Balta, J.B.; Barry, P.H.; Bodnar, R.J.; Taylor, L.A. Two-stage Polybaric Formation of the New Enriched, Pyroxene-oikocrystic, Lherzolitic Shergottite, NWA 7397. *Meteorit. Planet. Sci.* **2014**, *49*, 1812–1830. [CrossRef]
131. Mcsween, H.Y.; Treiman, A.H. Martian Meteorites. *Rev. Mineral. Geochem.* **1998**, *36*, 6-01–6-54.
132. Day, J.M.D.; Tait, K.T.; Udry, A.; Moynier, F.; Liu, Y.; Neal, C.R. Martian Magmatism from Plume Metasomatized Mantle. *Nat. Commun.* **2018**, *9*, 4799. [CrossRef]
133. Nicklas, R.W.; Day, J.M.D.; Vaci, Z.; Udry, A.; Liu, Y.; Tait, K.T. Uniform Oxygen Fugacity of Shergottite Mantle Sources and an Oxidized Martian Lithosphere. *Earth Planet. Sci. Lett.* **2021**, *564*, 116876. [CrossRef]
134. Udry, A.; Day, J.M.D. 1.34 Billion-Year-Old Magmatism on Mars Evaluated from the Co-Genetic Nakhlite and Chassignite Meteorites. *Geochim. Cosmochim. Acta* **2018**, *238*, 292–315. [CrossRef]
135. Tutolo, B.M.; Tosca, N.J. Observational Constraints on the Process and Products of Martian Serpentinization. *Sci. Adv.* **2023**, *9*, eadd8472. [CrossRef]
136. Neuendorf, K.E.; Mehl, J.P., Jr.; Jackson, J.A. (Eds.) *Glossary of Geology*, 5th ed.; American Geosciences Institute: Alexandria, VA, USA, 2011; ISBN 9780922152896. Available online: https://www.abebooks.com/9780922152896/Glossary-Geology-Fifth-Edition-revised-0922152896/plp (accessed on 4 March 2024).
137. Blake, D.F.; Sarrazin, P.; Bristow, T.F.; Treiman, A.H.; Zacny, K.; Morrison, S. Progress in the Development of CheMin-V, a Definitive Mineralogy Instrument for Landed Science on Venus. In Proceedings of the 19th Meeting of the Venus Exploration Analysis Group (VEXAG), Virtual, 8–9 November 2021; 2628. p. 8032.
138. Blake, D.F.; Treiman, A.; Sarrazin, P.; Bristow, T.S.; Downs, R.; Yen, A.; Zacny, K. CHEMIN-V: A Definitive Mineralogy Instrument for Landed Venus Science. In Proceedings of the 51st Lunar and Planetary Science Conference, The Woodlands, TX, USA, 16–20 March 2020; p. 1814.
139. Blake, D.; Hazen, R.M.; Morrison, S.M.; Bristow, T.S.; Sarrazin, P.; Zacny, K.; Rampe, E.B.; Downs, R.T.; Yen, A.; Ming, D.W.; et al. In-Situ Crystallographic Investigations of Solar Systems in the next Decade. *Bull. AAS* **2021**, *53*, 131. [CrossRef]
140. Blake, D.; Bristow, T.; Sarrazin, P.; Zacny, K. In-Situ Mineralogical Analysis of the Venus Surface Using X-ray Diffraction. *Bull. AAS* **2021**, *53*, 1–7. [CrossRef]
141. Morrison, S.; Pan, F.; Prabhu, A.; Eleish, A.; Fox, P.; Gagne, O.; Downs, R.; Bristow, T.; Rampe, E.; Blake, D.; et al. Machine Learning in Predicting Multi-Component Mineral Compositions in Gale Crater, Mars. In Proceedings of the Goldschmidt Conference 2019, Barcelona, Spain, 18–23 August 2019; p. 2343.
142. Eleish, A.; Morrison, S.M.; Pan, F.; Prabhu, A.; Downs, R.T.; Rampe, E.B.; Castle, N.; Blake, D.F.; Bristow, T.; Hazen, R.; et al. Predicting Multi-Component Mineral Compositions from Crystallographic Parameters Using Machine Learning for Spacecraft X-ray Diffraction Instruments. In Proceedings of the AGU Fall Meeting 2023, San Francisco, CA, USA, 11–15 December 2023.
143. Geng, X. Label Distribution Learning. *IEEE Trans. Knowl. Data Eng.* **2016**, *28*, 1734–1748. [CrossRef]
144. Morrison, S.; Pan, F.; Gagné, O.; Prabhu, A.; Eleish, A.; Fox, P.; Downs, R.; Bristow, T.; Rampe, E.; Blake, D.; et al. Predicting Multi-Component Mineral Compositions in Gale Crater, Mars with Label Distribution Learning. In Proceedings of the AGU Fall Meeting Abstracts, Washington, DC, USA, 10–14 December 2018; p. P21I-3438.
145. Hazen, R.M.; Morrison, S.M.; Prabhu, A.; Williams, J.; Wong, M.; Krivovichev, S.V.; Bermanec, M. On the Attributes of Mineral Paragenetic Modes. *Can. J. Mineral. Petrol.* **2023**, *61*, 653–673. [CrossRef] [PubMed]
146. Bristow, T.F.; Haberle, R.M.; Blake, D.F.; Des Marais, D.J.; Eigenbrode, J.L.; Fairén, A.G.; Grotzinger, J.P.; Stack, K.M.; Mischna, M.A.; Rampe, E.B.; et al. Low Hesperian PCO2 Constrained from in Situ Mineralogical Analysis at Gale Crater, Mars. *Proc. Natl. Acad. Sci. USA* **2017**, *114*, 2166–2170. [CrossRef] [PubMed]
147. Jennings, E.S.; Coull, P. Olivine Microstructure and Thermometry in Olivine-phyric Shergottites Sayh al Uhaymir 005 and Dar al Gani 476. *Meteorit. Planet. Sci.* **2024**, *59*, 55–67. [CrossRef]
148. Dreibus, G.; Wa, H. Volatiles on Earth and Mars: A Comparison. *Icarus* **1987**, *71*, 225–240. [CrossRef]
149. Helffrich, G. Mars Core Structure—Concise Review and Anticipated Insights from InSight. *Prog. Earth Planet. Sci.* **2017**, *4*, 24. [CrossRef]
150. Gilmore, M.; Treiman, A.; Helbert, J.; Smrekar, S. Venus Surface Composition Constrained by Observation and Experiment. *Space Sci. Rev.* **2017**, *212*, 1511–1540. [CrossRef]
151. Weber, I.; Morlok, A.; Bischoff, A.; Hiesinger, H.; Ward, D.; Joy, K.; Crowther, S.; Jastrzebski, N.; Gilmour, J.D.; Clay, P.; et al. Cosmochemical and Spectroscopic Properties of Northwest Africa 7325—A Consortium Study. *Meteorit. Planet. Sci.* **2016**, *51*, 3–30. [CrossRef]
152. Cloutis, E.A. Seeing Through the Atmosphere of Venus: What Is on the Surface? *Geophys. Res. Lett.* **2021**, *48*, e2020GL092128. [CrossRef]
153. Bott, N.; Brunetto, R.; Doressoundiram, A.; Carli, C.; Capaccioni, F.; Langevin, Y.; Perna, D.; Poulet, F.; Serventi, G.; Sgavetti, M.; et al. Effects of Temperature on Visible and Infrared Spectra of Mercury Minerals Analogues. *Minerals* **2023**, *13*, 250. [CrossRef]